International Journal of Solids and Structures 120 (2017) 81–102

Contents lists available at ScienceDirect

International Journal of Solids and Structures

journal homepage: www.elsevier.com/locate/ijsolstr

Continuous chip formation in metal cutting processes using the Particle Finite Element Method (PFEM)

J.M. Rodríguez [a,*], J.M. Carbonell [c], J.C. Cante [b,c], J. Oliver [c]

[a] Division of Mechanics of Solid Materials, Luleå University of Technology (LTU), Sweden
[b] Escola Tècnica Superior d'Enginyeries Industrial i Aeronàutica de Terrassa, Rambla de Sant Nebridi 22, 08222 Terrassa, Spain
[c] International Center for Numerical Methods in Engineering (CIMNE), Campus Nord UPC, Gran Capitán, s/n., 08034 Barcelona, Spain

ARTICLE INFO

Article history:
Received 13 October 2016
Revised 29 March 2017
Available online 21 April 2017

Keywords:
Particle Finite Element Method (PFEM)
Metal cutting processes

ABSTRACT

This paper presents a study on the metal cutting simulation with a particular numerical technique, the Particle Finite Element Method (PFEM) with a new modified time integration algorithm and incorporating a contact algorithm capability . The goal is to reproduce the formation of continuous chip in orthogonal machining. The paper tells how metal cutting processes can be modelled with the PFEM and which new tools have been developed to provide the proper capabilities for a successful modelling. The developed method allows for the treatment of large deformations and heat conduction, workpiece-tool contact including friction effects as well as the full thermo-mechanical coupling for contact. The difficulties associated with the distortion of the mesh in areas with high deformation are solved introducing new improvements in the continuous *Delaunay* triangulation of the particles. The employment of adaptative insertion and removal of particles at every new updated configuration improves the mesh quality allowing for resolution of finer-scale features of the solution. The performance of the method is studied with a set of different two-dimensional tests of orthogonal machining. The examples consider, from the most simple case to the most complex case, different assumptions for the cutting conditions and different material properties. The results have been compared with experimental tests showing a good competitiveness of the PFEM in comparison with other available simulation tools.

1. Introduction

1.1. Description of the problem

The metal cutting in machining is a process in which a thin layer of metal, the chip, is removed from the surface of a body by the action of a wedge-shaped tool. Metal cutting processes are present in big industries that manufacture products with large size components (i.e. automotive industry, aerospace industry, home appliance industry, etc.), and also in high tech industries where small pieces are machined with high precision tolerances. The importance of machining is such that, it is the most common used process for producing components with specified geometrical dimensions and a determined quality in the surface finish. Its cost represent around 15% of the value of all manufactured products in all industrialized countries (Childs et al., 2000).

Cutting is a complex physical process in which phenomena of friction, adiabatic shear bands, excessive heating, large strains and high strain rates are involved. The characteristics of the tool shape, the tip, the rake and flank angles, and the cutting speed, among others, play a very important role in the generated cutting forces, the energy consumption, the tool wear and the obtained chip morphology from the cut. A lot of parameters and combinations are possible to design the proper cut for the machining of a metal piece. The study of metal cutting is difficult from an experimental point of view, experiments are difficult to carry out. Among the reasons there are the high speed at which the cut takes place when reproduce industrial machining conditions and the small scale of the phenomena of interest that have to be observed. Furthermore, the continuous development in the tool industry related to new materials and geometries and the introduction of new materials also for the workpieces make the experimental testing a laborious and hard task.

* Corresponding author.
E-mail addresses: man_rod1@hotmail.com (J.M. Rodríguez), cpuigbo@cimne.upc.edu (J.M. Carbonell).

http://dx.doi.org/10.1016/j.ijsolstr.2017.04.030

When modeling a machining processes using numerical simulation, the used method needs certain capabilities (see Rakotomalalan et al. (1993); Peri and Owen (1999); Sekhon and Chenot (1993); Marusich and Ortiz (1995); Limido et al. (2007)). Looking at what happens to the workpiece, the material is highly deformed due to the cutting. This is translated to the modelling as large mesh distortions if a *Lagrangian* mesh is considered. Therefore, modeling a machining process becomes a major challenge for the finite element method (FEM). A *Langrangian* FEM without remeshing cannot resolve the large deformations very well. Element distortion has been always matter of concern which limited the analysis to incipient chip formation in some studies. Instead, FEM with an *Eulerian* formulation requires the knowledge of the chip geometry in advance, that, undoubtedly, restricts the range of cutting conditions capable of being analyzed. In order to avoid the disadvantages of Finite Element Lagrangian and Eulerian formulations, other computational techniques have been investigated. One of them is the Finite Element Arbitrary Lagrangian Eulerian (ALE) formulation in conjunction with adaptive mesh techniques (Rakotomalalan et al., 1993; Gadala et al., 2002; Gadala, 2004; Olovsson et al., 1999). The ALE formulation combines the best features of pure Lagrangian analysis (in which the mesh follows the material) and Eulerian analysis (in which the mesh is fixed and the material flows though the mesh).

The main goal of this work is precisely make a contribution to the solution of some of the problems described above through the significant extension and improvement of the Particle Finite Element Method (PFEM) to thermo-mechanical problems with large deformations. This is done by means of the use of the theory of solid mechanics and taking into account finite strains and rotations, multiple contacts and generation of new surfaces. The objective is focused in the numerical simulation of metal cutting processes. In this work, we exploit the particle and *Langrangian* nature of PFEM and the advantages of finite element discretization to study the formation of continuous chip shapes in steel. We are going to employ different numerical techniques for the treatment of contact, for the constitutive modelling of the metal-like materials as well as for the integration of the governing equations. Machining at different cutting speeds and with different tool geometries are analyzed in order to define the proper numerical modelling for the simulation of continuous chip formation in metal cutting.

We start presenting the PFEM in Section 2, the basic general steps and the custom characteristics used in the present formulation are explained. In Section 3 the coupled thermo-mechanical problem is described with a summarized form of the balance equations of the initial boundary value problem (IBVP). The equations are presented using the weak form of the problem and particularized with the mixed displacement-pressure formulation which prompted the use of stabilization.

In Section 4 we present an overview of the thermo-elastoplastic models at finite strains used to reproduce the continuous cut and also we present a novel Impl-Ex integration scheme of the constitutive equations (Oliver et al., 2008). In Section 5 we describe the contact phenomena at the workpiece-tool interface with a rigid and a deformable models for the cutting tool. A constitutive law for the frictional contact and the heat generation and transfer are described in this section.

In Section 6, we present a new staggered algorithm, which is based on the isothermal split presented in Simo and Miehe (1992) and the Impl-Ex integration scheme of the constitutive equations presented in Oliver et al. (2008). The models presented in Sections 4 and 5 will be used in the examples of Section 7 to test the capabilities of the present formulation in problems of industrial interest.

2. The Particle Finite Element Method

The Particle Finite Element Method (PFEM) was developed first for the treatment of fluids (Idelsohn et al., 2004). The aim was to model free surfaces in a Lagrangian manner, following and tracking the fluid particles along the domain. The Lagrangian description of the continuum was usually applied to solids opening the possibilities of application to the modelling of fluid structure interaction and coupled problems. A wide range of simulations has been faced with PFEM: fluid interacting with rigid bodies, used in marine and port engineering; erosion processes, used in river engineering, mixing processes or fluid coupling with thermal effects; trying to give a response to many industrial problems (Onate et al., 2008; 2006; Franci, 2015).

As described previously, in this paper we modify and improve the PFEM, presenting as a result a new approach to the modelling of industrial cutting processes. This is within the theory of solids where the Lagrangian description of the continuum is something more common. However finite elements have some critical limitations they deform too much and its shape is distorted. That occurs when the material suffers large strains as in the concerning problem. The role of the particle description is to solve this matter.

The original idea of the PFEM was to improve the mesh quality by performing a re-triangulation of the domain only when is needed, which allows to capture large changes in the continuum domain and avoid global remeshing and interpolation from mesh to mesh. Usually, that is performed according to some criteria associated to element distortion. In 2D, the re-triangulation consists in re-computing the element connectivity using a *Delaunay* triangulation (Delaunay, 1934; Shewchuk, 1998) where the current position of the particles (i.e., of the mesh nodes) is kept fixed. Mesh distortion is corrected and improved naturally with the PFEM, because the triangulations maximize the minimum angle of all the angles of the triangles in the triangulation. Therefore, they tend to avoid skinny triangles.

We must mention here that first applications of the PFEM to solid mechanics were done in problems involving large strains and rotations, multi body contacts and creation of new surfaces (riveting, powder filling and machining) (Oliver et al., 2007; Rodriguez, 2014; Rodriguez et al., 2015). In this work, we extended the Particle Finite Element Method to the numerical simulation of metal cutting processes.

A summary about the basis of the standard PFEM is presented in Appendix A. An example of the remeshing scheme using PFEM is shown in Fig. 1.

2.1. Meshing procedure and variables transfer in the PFEM

The basic steps of the PFEM describe the importance of the meshing procedure which is performed via *Delaunay* triangulation. This strategy has some important implications, the *Delaunay* triangulation generates the convex figure of minimum area that encloses all the points of the domain but that may be not conformal with the external boundaries of the solid domain. In fluids, the tracking of the free surfaces (the domain boundaries) is a part of the method capabilities and the boundary recognition problem is overcome with the so-called α-shape method (Edelsbrunner and Mucke, 1994). With the α-shape method one can consider that an element of the convex hull conforms an external boundary if fulfills a certain characteristic mesh size. That solves the problem partially, because the resultant external surface generated using α-shapes will be different from the previous known external boundaries. That may affect the volume conservation of the domain analyzed which is a relevant weakness when it is applied to solid mechanics problems.

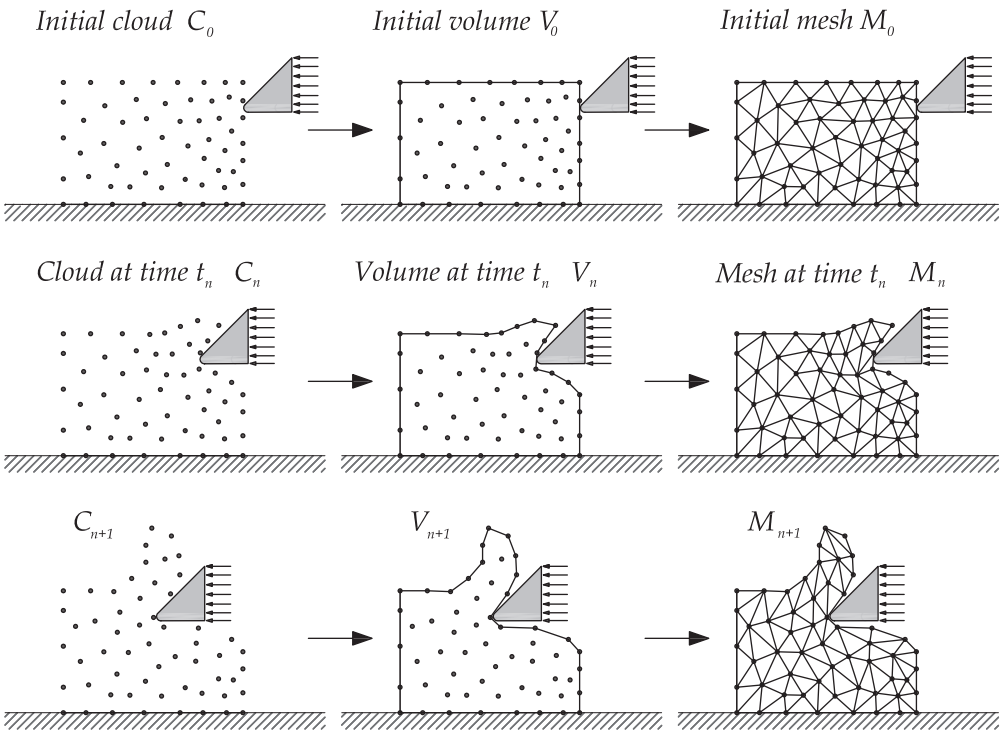

Fig. 1. Remeshing steps in a standard PFEM numerical simulation.

To deal with this problem, in this work, we propose the use of a constrained *Delaunay* algorithm (Delaunay, 1934; Shewchuk, 1998). This may preserve the external boundaries and the volume conservation is guaranteed. There also exist other solutions to preserve the contour surface and the volume of the model using a non-constrained *Delaunay* tessellation. That solutions consist in techniques that combine the α-shapes with the previous boundary magnitudes, like normals and directions, that applied properly also preserve the contour surface and the volume of the model (Carbonell, 2009). Note that in order to deal with complex material flows, where the material can be merged, the use of α-shapes will be essential. Furthermore, the use of α-shapes also allows the extension to 3D models where, in many cases, the constrained *Delaunay* tessellation is not guaranteed. Although, in certain non-convex domains, where the constrained tessellation is not allowed, one possible solution consists in adding some nodes on the border of the domain. The addition and removal of particles is one of the used tools in the presented meshing procedure for the PFEM.

In the Lagrangian approach, the particles move because of the material flow and it may happen that particles concentrate in same regions of the domain and, on the contrary, in other regions the number of particles becomes too low to obtain an accurate solution. To overcome these difficulties, basic PFEM adds and removes particles comparing with a certain characteristic distance h (the size is problem depend and usually constant along the domain) (see Cremonesi (2010); Cremonesi et al. (2010a)). If the distance between two nodes d_{nodes} is $d_{\text{nodes}} < h$, one of the nodes is removed. If the radius of an element circumsphere r_{ec} is $r_{\text{ec}} > h$, a new node is added at the center of the circumsphere. The flow variables in the new node are linearly interpolated from that of the element nodes, and the assigned material properties are the ones of the elements.

The addition and removal of particles is one of the principal tools that we have extended into the PFEM. By inserting and removing particles, the main difficulties associated with element distortion, can be solved and it also allows for the resolution the different scales of the solution. The addition and removal of particles improve the quality of the solution, and allows us to reach a solution if the mesh is too coarse.

Removing particles

The removal of particles is based on geometrical criteria and physical error estimators. First, if the distance between two nodes $d_{\text{nodes}} < h$ is smaller than certain characteristic distance h, one of the nodes will removed (see Fig. 2 in the middle). Second, if the error estimator $\|\sigma - \sigma_h\| < \varepsilon_{tol}$, a Zienkiewicz–Zhu error estimator (Zienkiewicz and Zhu, 1992a; 1992b), is smaller that a given tolerance ε_{tol}, the particle that is in the center of the patch is removed (see Fig. 2 in the left). The error estimators used are based on plastic strain values or on the norm of the isochoric-stress. Two magnitudes that describe the region of interest where the different scale of the physical solution is taking place. The absence of error on them says that nothing relevant occur in that zone and that the finite element mesh can be coarsened if needed.

Third, in the domain boundary, the removal of particles follows only the criterion based on a characteristic distance $d_{\text{nodes}} < h_{\text{s}}$ (see Fig. 2 in the right).

Adding particles

The insertion of particles we propose is based on the equidistribution of the plastic power, such that, elements exceeding the prescribed tolerance ε_{tol} are targeted for refinement.

$$\int_{\Omega^e} \mathcal{D}_{mech}\, d\,\Omega^e > \varepsilon_{tol} \tag{1}$$

where $\mathcal{D}_{mech}$ is the mechanical power (see Simo (1988a); 1988b)) and Ω^e is the domain of the element. When the condition is fulfilled, a particle is inserted in the Gauss point of the finite element. Here we also account for the basic mesh size refinement, that is if the radius of an element circumsphere mathec is $r_{\text{ec}} > h$, a new node is added at the center of the circumsphere.

In the domain boundary, the insertion of particles is a fundamental thing for metal cutting problems. The geometrical descrip-

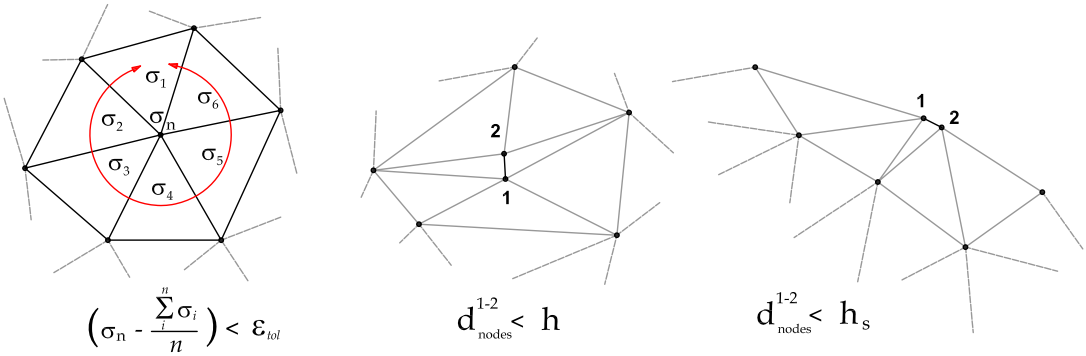

Fig. 2. Three main criteria to remove a particle.

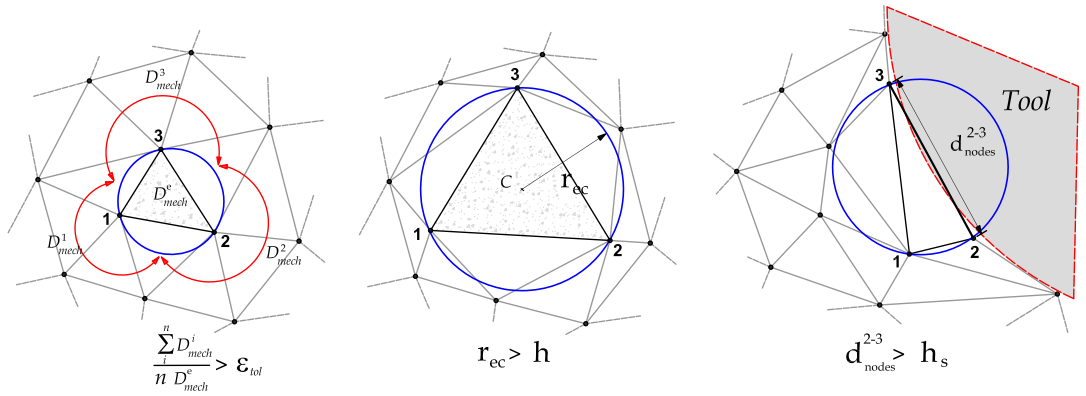

Fig. 3. Three main criteria to add a new particle.

tion of the cut is done by the insertion of particles in the boundary of the workpiece at the tool tip. This allows for the contour increase and creates the shape of the cut. The criterion used for the insertion of particles is based on a characteristic distance $d_{\text{nodes}} > h_s$. This characteristic distance h_s has a direct relationship with the geometrical resolution of the cutting tool tip, where the cut of the material is originated. The critical cases for the addition of new particles are depicted in Fig. (3).

Information transfer

In order to not destroy the finite element solution from one reconnection step to another, the transfer of the information is crucial. All the information necessary in subsequent time steps has to be transferred from the old mesh to the new mesh, it includes the nodal information like displacements, temperatures, pressure in the new inserted particles, and the Gauss point information like internal variables in the new element.

Particles preserve the information from mesh to mesh. Only in the case of the inserted particles an interpolation is needed to define their new nodal information. In the case of removed particles, the information stored in them is lost for the subsequent time steps, but it is kept until the end of the meshing procedure to perform the interpolations with fidelity. The coarsening of the mesh is useful to reduce the computational cost of the model, however is not always possible to coarsen the mesh if the information has to be preserved. One example of this are the residual stresses in the model. If the model is coarsened this information will be lost.

The loss of information is not only due to mesh coarsening also to the transfer of information between Gauss points. The classical PFEM transfer is focused in keeping the information in particles. It transfers the elemental values to particles and it recovers them later to Gauss points. This is a very diffusive process, even if you transfer only the increments of the elemental values. In the places where the mesh does not change the solution is smoothed anyway and the equilibrium information is lost. That not happens if the transfer is done directly from the previous element to the new element. If the information is transferred between elements, when mesh does not change, the solution is the same and the equilibrium is preserved. When the mesh is not the same, the equilibrium is perturbed only in areas where large changes occurred and the transformation of the information is unavoidable. A thermo-mechanical traction test was presented in a previous work (see Rodriguez et al. (2016)), where the solution using PFEM and FEM was compared, and as a result similar result were obtained, showing that the effect of transfer the internal variables from gauss point to gauss point as is done is the present work is negligible in problems similar to the ones presented in this work.

In Box 1, the procedure for mesh refinement and information transfer is shown. This procedure is the one that is applied in the simulation of metal cutting processes.

3. Description of the thermo-mechanical problem

Next we are going to describe the main equations describing the Initial Boundary Value Problem (IBVP), the variables that must be considered and as well as all terms and factors that we will need to solve it. This description is performed inside the theory of continuum mechanics.

3.1. Balance equations for the thermo-mechanical IBVP

Let **x** denote the current position of a solid particle in the current configuration at time t, $\mathbf{u}(\mathbf{x}, t)$ its displacement, $\theta(\mathbf{x}, t)$ its tem-

PFEM: MESH REFINEMENT
and
INFORMATION TRANSFER

1. Update the particle positions due to motion.

2. Remove particles. Criterion based on distances and error estimators. If at least one boundary particle is removed, reconstruct the boundary.

3. Refine boundary that is too distorted. Criterion based on distance. If at least one boundary particle is inserted, reconstruct the boundary.

4. Perform a constrained *Delaunay* triangulation. The triangulation must include remaining particles and preserve boundaries.

5. Refine elements. Criterion based on plastic dissipation values and distances.

6. Refine previous *Delaunay* triangulation. The new triangulation must include new particles and preserve the boundaries.

7. Calculate the global coordinates of the gauss points of the new triangulation.

8. Using the information of the previous mesh, update the internal variables of the new triangulation.

It is important to remark that step 2 is optional.
The main advantage of the proposed strategy is that:
It is not necessary to create a complete new mesh (without step 2); we only adapt the mesh with the addition of particles and the mesh quality is improved using a *Delaunay* triangulation. The insertion of particles takes places in the primary shear zone and in the boundary where the tool is in contact with the chip. The removal of particles takes place in the formed chip far from the primary shear zone.

Box 1. Flowchart of the refining scheme and information transfer process.

perature and $p(\mathbf{x}, t)$ its pressure. For a solid, the momentum, the mass conservation and the energy equations write in their weak forms as

$$\begin{aligned}
&\int_{V_t} \delta\varepsilon_{ij} s_{ij}\, dV_t + \int_{V_t} \delta\varepsilon_{ij} p\delta_{ij}\, dV_t - \int_{V_t} w_i b_i\, dV_t - \int_{\Gamma_N} w_i t_i^p d\Gamma = 0 \\
&\int_{V_t} -\frac{q}{\kappa}\, p\, dV_t + \int_{V_t} q\frac{\ln(J)}{J}\, dV_t = 0 \\
&\int_{V_t} \hat{w}\rho\, c\, \frac{d\theta}{dt}\, dV_t + \int_{V_t} \frac{\partial \hat{w}}{\partial x_i}(k\, \frac{\partial \theta}{\partial x_i})\, dV_t - \int_{V_t} \hat{w}\, (\sigma : \mathbf{d})\, dV_t \\
&\quad - \int_{V_t} \hat{w}\, Q\, dV_t + \int_{\Gamma_{N_\theta}} \hat{w} q_n^p\, d\Gamma = 0
\end{aligned} \tag{2}$$

where V_t is the volume occupied by the solid in the current configuration, s_{ij} is the deviatoric part of the Cauchy stress tensor and p is the pressure, b_i are the external body forces and t_i^p the prescribed surface forces, $\delta\varepsilon_{ij}$ is a virtual strain field and w_i are the space weighting functions for the displacement field.

In the second equation, J is the determinant of the deformation gradient and κ is the incompressibility modulus, q are the space weighting functions for the pressure. Finally in the third equation, θ is the temperature, ρ is the density, and c the specific heat, and k the thermal conductivity. Q is the thermal source and q_n^p the flux in the boundary. $\hat{w}$ are the space weighting functions for the temperature.

The initial conditions are prescribed assigning the initial displacement $\mathbf{u}_0(\mathbf{x})$, initial velocity $\mathbf{v}_0(\mathbf{x})$ and initial temperature $\boldsymbol{\theta}_0(\mathbf{x})$ at whereas both Dirichlet and Neumann type boundary conditions are imposed as:

$$\begin{aligned}
&\mathbf{u}(\mathbf{x}, t) = \bar{\mathbf{u}}(\mathbf{x}, t)\ \forall \mathbf{x} \in \Gamma_D \\
&\mathbf{v}(\mathbf{x}, t) = \bar{\mathbf{v}}(\mathbf{x}, t)\ \forall \mathbf{x} \in \Gamma_D \\
&\theta(\mathbf{x}, t) = \bar{\theta}(\mathbf{x}, t)\ \forall \mathbf{x} \in \Gamma_{D_\theta} \\
&\sigma(\mathbf{x}, t) \cdot \mathbf{n} = \bar{\mathbf{h}}(\mathbf{x}, t)\ \forall \mathbf{x} \in \Gamma_N \\
&-k\nabla\theta \cdot \mathbf{n} = \bar{\mathbf{q}}(\mathbf{x}, t)\ \forall \mathbf{x} \in \Gamma_{N_\theta}
\end{aligned} \tag{3}$$

where $\bar{\mathbf{u}}(\mathbf{x}, t), \bar{\mathbf{v}}(\mathbf{x}, t), \bar{\theta}(\mathbf{x}, t)$, $\bar{\mathbf{h}}(\mathbf{x}, t)$ and $\bar{\mathbf{q}}(\mathbf{x}, t)$ are assigned functions, $\mathbf{n}$ denotes the out-ward normal to the boundary and $\Gamma_D \cup \Gamma_N = \partial\Omega$ and $\Gamma_{DT} \cup \Gamma_{NT} = \partial\Omega$.

3.2. Stabilization of the mixed displacement-pressure equation

The monolithic approach of the mixed displacement-pressure problem, Eq. (2), fails to satisfy the inf-sup condition when equal order interpolants are used for both displacement and pressure fields. When the order of interpolation of the pressure field of the finite element is the same as the order of interpolation of the displacement field, the solution presents nonphysical oscillations.

Several techniques have been developed to address this problem, among them: The Characteristic Based Split (CBS) (Chorin, 1997), the finite calculus (FIC) (Onate et al., 2004), the Orthogonal Subgrid Scales (OSS) (Saracibar et al., 2006; Chiumenti et al., 2002; 2003) and the Polynomial Pressure Projection (PPP) (Dohrmann and Bochev, 2004; Bochev et al., 2008).

The so-called Polynomial Pressure Projection(PPP) technique is used in this work because it can be implemented in an elementary level surpassing the need of mesh dependent and problem dependent parameters (more information is given in Appendix B.

The stabilized set of governing equations for the displacement, pressure and temperature variables take the form:

$$\begin{aligned}
&\int_{V_t} \delta\varepsilon_{ij} s_{ij}\, dV_t + \int_{V_t} \delta\varepsilon_{ij} p\delta_{ij}\, dV_t - \int_{V_t} w_i b_i\, dV_t - \int_{\Gamma_N} w_i t_i^p d\Gamma = 0 \\
&\int_{V_t} -\frac{q}{\kappa}\, p\, dV_t + \frac{\ln(J)}{J}\int_{V_t} q\frac{\ln(J)}{J}\, dV_t + \int_{V_t} (q-\check{q})\frac{\alpha_s}{\mu}(p-\check{p}) dV_t = 0 \\
&\int_{V_t} \hat{w}\rho\, c\, \frac{d\theta}{dt}\, dV_t + \int_{V_t} \frac{\partial \hat{w}}{\partial x_i}(k\, \frac{\partial \theta}{\partial x_i})\, dV_t - \int_{V_t} \hat{w} Q\, dV_t \\
&\quad - \int_{V_t} \hat{w}\, (\sigma : \mathbf{d})\, dV_t + \int_{\Gamma_{N_\theta}} \hat{w} q_n^p\, d\Gamma = 0
\end{aligned} \tag{4}$$

where α_s is the stabilization parameter ($\alpha_s = 1$ for all the numerical simulations presented in this work), μ is the material shear modulus and $\check{p}$ is the best approximation of the pressure p in the space of polynomials of order $\mathcal{O}(Q^0)$.

They completed by adding the proper initial conditions and constraint equations related to the problem variables as described in 3.

4. Constitutive modelling of a metal-like material

The type of modelling that we are going to analyze in this work needs for the treatment of plasticity. The elastic behaviour is considered non-linear and the thermal effects, like the generation of heat, must also be taken into account in the constitutive law.

4.1. Thermo-hyperelastoplasticity at finite strains

The starting model is an hyperelastic model under temperature effects. We must consider material isotropy and assume that also in the thermal response. Volumetric changes in the constitutive response must be accounted due to the variation of the temperature in the material.

The Neo-Hookean material used to represent the phenomenology mentioned above is represented with the following free energy function, (see Bonet and Wood (1997); Simo (1988a).

$$\psi(\mathbf{b}) = U(J) + W(\mathbf{b}) + M(\theta, J) \tag{5}$$

The elastic part of the free energy is uncoupled into volumetric/deviatoric response described by the functions $U(J)$ and $W(\mathbf{C})$, respectively. The function $M(\theta, J)$ describes the thermo-mechanical coupling due to thermal expansion and provides the potential for the associated elastic structural entropy.

Consistent with the assumption of isotropy and extending the hyperelastic model to plasticity we characterize the stress response by a stored energy with the form

$$\psi = U(J^e) + W(\bar{\mathbf{b}}^e) + M(\theta, J^e) + T(\theta) + K(\bar{e}^p, \theta) \tag{6}$$

In this case the function $T(\theta)$ is the potential for the purely thermal entropy. The function $K(\bar{e}^p, \theta)$ is a nonlinear function of the equivalent plastic strain $\bar{e}^p$ and temperature θ which describes the isotropic strain hardening via the relation $\beta = -\partial_{\bar{e}^p} K(\bar{e}^p, \theta)$. To make matters as concrete as possible, we consider the following explicit forms (Simo and Miehe, 1992; Čanadija and Brnić, 2004).

$$\begin{aligned}
&U(J^e) = \frac{1}{2}\kappa \ln^2(J^e) \\
&W(\bar{\mathbf{b}}^e) = \frac{1}{2}\mu\left[tr(\bar{\mathbf{b}}^e) - 3\right] = \frac{1}{2}\mu\left[tr(\bar{\mathbf{C}}^e) - 3\right] \\
&T(\theta) = c\left[(\theta - \theta_0) - \theta \ln\left(\frac{\theta}{\theta_0}\right)\right] \\
&M(\theta, J^e) = -3\,\alpha\,\kappa\,\frac{\ln(J^e)}{J^e}(\theta - \theta_0)
\end{aligned} \tag{7}$$

where $\mu > 0$, $\kappa > 0$, $c > 0$ and α can be interpreted as the shear modulus, the bulk modulus, the heat capacity and the thermal expansion coefficient,respectively. $\bar{\mathbf{b}}^e$, $\bar{\mathbf{C}}^e$ and J^e are the elastic left Cauchy–Green tensor, the elastic right Cauchy–Green tensor and the determinant of elastic deformation tensor $\mathbf{F^e}$, respectively.

4.2. Yield condition

Accurate flow stress models are considered extremely necessary to represent work material constitutive behavior under high strain rate deformation conditions. We consider the classical *Mises–Hubber* yield conditions, expressed in terms of the Kirchhoff stress tensor, for the case of rate independent plasticity:

$$\begin{aligned}\Phi(\tau,\bar{e}^{\,p},\theta) &= \|dev(\tau)\| - \sqrt{\frac{2}{3}}\big(\sigma_y - K'(\bar{e}^{\,p},\theta)\big)\\ &= \|dev(\tau)\| - \sqrt{\frac{2}{3}}(\sigma_y+\beta) \le 0\end{aligned} \tag{8}$$

and for rate dependent plasticity

$$\begin{aligned} f(\tau,\bar{e}^{\,p},\theta) &= \|dev(\tau)\| - \sqrt{\frac{2}{3}}(\sigma_y+\beta)\Big(1+g(\dot{\bar{e}}^{\,p})\Big) = 0\\ &\text{or}\\ f(\tau,\bar{e}^{\,p},\theta) &= \Phi(\tau,\bar{e}^{\,p},\theta) - \sqrt{\frac{2}{3}}(\sigma_y+\beta)g(\dot{\bar{e}}^{\,p}) = 0\\ &\text{if } \Phi(\tau,\bar{e}^{\,p},\theta) > 0\end{aligned} \tag{9}$$

where σ_y denotes the flow stress, $\beta = -K'(\bar{e}^{\,p},\theta)$ the isotropic nonlinear hardening modulus, $g(\dot{\bar{e}}^{\,p})$ the strain rate hardening modulus. The expressions $(\sigma_y+\beta)$ y and $g(\dot{\bar{e}}^{\,p})$ depend on the hardening law used. Numerous empirical and semi-empirical flow stress models have been proposed. The strain-rate dependent model developed by Johnson and Cook (1983) and the rate independent model developed by Voce (1955) will be used in this work.

4.3. Isotropic hardening laws

In a typical machining event, very high strain rates in excess of 10^5 may be attained within the primary shear zone, while the remainder of the workpiece deforms at moderate or low strain rates. A simple model which accounts for this behavior is the *Johnson and Cook* strength model. For the sake of comparison, next we present the rate independent hardening law developed by Voce (1955) and rate dependent hardening law developed by *Johnson and Cook*. Both hardening laws are usually applied in the numerical simulation of machining processes.

4.3.1. Voce *strength model*

Voce (1955) proposed an exponential form of hardening. This assumes that the hardening eventually reaches a specified saturation (or maximum) stress. The strain hardening law interrelating true stress σ_y and true plastic strain $\bar{\varepsilon}_p$ is expressed as

$$(\sigma_y+\beta) = (K_{\inf} - (K_{\inf}-\sigma_0)e^{-\delta\bar{\varepsilon}_p} + H\bar{\varepsilon}) * (1 - w_0(\theta-\theta_0)) \tag{10}$$

where K_{inf} is the saturation stress, σ_0 is the true stress at the onset of plastic deformation and H is the linear hardening modulus. The constant δ determines the rate at which the stress σ_0 moves from its initial value tends to reach steady state or saturation stress K_{inf}. The material property w_0 describes the thermal softening of the material of interest. The dependency of the hardening law on the temperature represents the softening of the material when its temperature is increased. The Voce model describes the strain hardening and thermal softening of most steels in the temperature range 300K to 400K and at low strain rates. Extended information can be found in Simo and Miehe (1992).

A material model that describes the behavior of metal in a wide range of temperatures, strain and strain rates is explained in the next.

4.3.2. Johnson-Cook *strength model*

The *Johnson-Cook* strength model is a phenomenological model. Under certain conditions, the flow stress of some materials was observed to behave in a manner that could be described reasonably well by particular mathematical forms. The *Johnson-Cook* model describes the flow of the material as the product of three mathematical terms with A, the initial yield strength of the material at room temperature and a reference strain rate.

$$(\sigma_y+\beta) = A\Big(1+\frac{B}{A}\varepsilon^n\Big)\big(1+C\ln\dot{\varepsilon}'\big)(1-\theta'^m) \tag{11}$$

Here, ε is the equivalent plastic strain, $\dot{\varepsilon}'$ is the strain rate nondimensionalized by the reference strain rate, and B, C, m and n are fitting constants. It is important to remark that, that if $n = 1$, $m = 1$ and $C = 0$, the *Johnson-Cook* material model recovers the Voce model.

4.4. Associative flow rule

The functional form of the corresponding associate flow rule is uniquely determined analyzing the evolution equations and the plastic dissipation. For the *Mises–Hubber* yield function (9) and the free energy function (6), Simo and Miehe (1992) and Ibrahimbegovic and Chorfi (2002) show that the flow rule takes the form based on the principle of maximum plastic dissipation. A summary of the J_2-plastic flow model with isotropic hardening is shown in Box 2. In this model, we assume that the deformation gradient $\mathbf{F}$ admit a multiplicative decomposition in elastic and plastic parts, $\mathbf{F} = \mathbf{F^e F^p}$, respectively. The elastic response is expressed in terms of $\mathbf{b^e} = \mathbf{F^e F^{eT}}$, where $\mathbf{b^e}$ is the elastic left Cauchy–Green deformation tensor.

The main equations for the constitutive model introduced here will be integrated using a new scheme for thermo-hyperelastoplasticity called IMPL-EX scheme, see Oliver et al. (2008).

4.5. Time integration of the constitutive law: The IMPL-EX integration scheme

In this section we focus in the problem of integrating numerically the initial-value ODE equations configured by the Evolution equations and the *Kuhn–Tucker* conditions (see Box 2).

The implicit Backward-Euler method is the most commonly used integration scheme for plasticity (see Simo (1988a); 1988b); Simo and Hughes (1998)) . Although the convergence of the integration is guaranteed, the fully implicit integration of the constitutive law requires some relevant computational effort and can experience some numerical problems of robustness when the material failure appears.

To improve the performance in the integration of the constitutive law, we introduce the integration of the constitutive law by means of the IMPL-EX scheme. Next, we develop the IMPL-EX integration for the thermo-hyperelastoplastic constitutive model used in this work.

We simply choose the variable to be treated explicitly and the stress update algorithm arising from this choice must be derived. By definition, the equivalent plastic strain is a monotonically increasing function of time, $\dot{\bar{e}}^{\,p} \ge 0$. For this reason, it is a logical candidate to be treated explicitly, since its evolution can be predicted

Coupled Thermo-Mechanical J_2 Flow Theory

1. Free energy function.

$$\psi = T(\theta) + M(\theta, J^e) + U(J^e) + W(\bar{\mathbf{b}}^e) + K(\bar{e}^{\,p}, \theta)$$

2. Kirchhoff stress.

$$\begin{aligned} \boldsymbol{\tau} &= J^e\, p\, \mathbb{1} + \mathbf{s} \\ p &:= \left[-3\,\alpha\,\kappa\, \frac{(1-\ln(J^e))}{J^e}(\theta-\theta_0) + \kappa\, \ln(J^e) \right] \\ \mathbf{s} &:= \mu\, dev(\bar{\mathbf{b}}^e) \end{aligned}$$

and the entropy

$$\begin{aligned} \eta &= \eta^p - \eta^e + \eta^t \\ \eta^e &:= -\partial_\theta T(\theta) \\ \eta^t &:= -\partial_\theta M(\theta, J^e) - \partial_\theta K(\bar{e}^{\,p}, \theta) \end{aligned}$$

3. *von Mises* yield criterion.

$$\Phi(\tau, \bar{e}^{\,p}, \theta) = \|dev(\tau)\| - \sqrt{\frac{2}{3}}\,(\sigma_y + \beta) \leq 0$$

4. Evolution equations $\lambda > 0, \quad \Phi \leq 0, \quad \lambda\,\Phi = 0$

$$\begin{aligned} \mathcal{L}_v \mathbf{b}^e &= -2\,\lambda\, J^{-\frac{2}{3}} \frac{1}{3} tr(\bar{\mathbf{b}}^e)\mathbf{n} \\ \dot{\bar{e}}^{\,p} &= -\lambda\, \partial_\beta \Phi(\tau, \bar{e}^{\,p}, \theta) \\ \dot{\eta}^p &= \lambda\, \partial_\theta \Phi(\tau, \bar{e}^{\,p}, \theta) \end{aligned}$$

The definition of the variables that appear in this box are explained in references (Simo and Hughes (1998); Simo (1988a); Simo (1988b))

Box 2. Coupled thermo-mechanical J_2 flow theory.

more accurately than other variables exhibiting non-monotonic behavior.

Using the Taylor expansion of the equivalent plastic strain at t_{n-1} around t_n we can find an explicit extrapolation formula of the equivalent plastic strain. Expression (12) constitutes an explicit extrapolation of the equivalent plastic strain at t_{n+1} in terms of the implicit values computed at t_n and t_{n-1}.

$$\tilde{\bar{e}}^{\,p}_{n+1} = \bar{e}^{\,p}_n + (\bar{e}^{\,p}_n - \bar{e}^{\,p}_{n-1})\,\frac{\Delta t_{n-1}}{\Delta t_n} \tag{12}$$

The Impl-Ex algorithm is a multistep method, since two points are used to advance the solution in time to point t_{n+1}.

The algorithmic plastic multiplier resulting from this extrapolation reads:

$$\begin{aligned} \Delta\tilde{\lambda}_{n+1} &= \sqrt{\frac{3}{2}}(\tilde{\bar{e}}^{\,p}_{n+1} - \bar{e}^{\,p}_n) \\ &= \sqrt{\frac{3}{2}}(\bar{e}^{\,p}_n - \bar{e}^{\,p}_{n-1})\frac{\Delta t_{n+1}}{\Delta t_n} \\ &= \Delta\lambda_n \frac{\Delta t_{n+1}}{\Delta t_n} \end{aligned} \tag{13}$$

Expression (13) reveals that the elastic or plastic nature of the response predicted by the Impl-Ex integration scheme at t_{n+1} is dictated by the response computed implicitly at t_n. This may give rise to overshoots and oscillations in the transitions from elastic to

Impl-Ex Integration Flowchart

1. Explicit extrapolation stage:

   Initial data: $\bar{\mathbf{b}}^e_n$, $\bar{e}^{\,p}_n$, η^p_n

   Current values of $\mathbf{F}_{n,n+1}$, θ_{n+1}

$$\begin{aligned} \Delta\tilde{\lambda}_{n+1} &= \sqrt{\frac{3}{2}}\Delta\lambda_n \frac{\Delta t_{n+1}}{\Delta t_n} \\ \tilde{\bar{e}}^{\,p}_{n+1} &= \bar{e}^{\,p}_n + \sqrt{\frac{2}{3}}\Delta\tilde{\lambda}_{n+1} \end{aligned}$$

2. Let $\bar{\mathbf{F}}_{n,n+1} = J^{-\frac{1}{3}}\mathbf{F}_{n,n+1}$ and set:

$$\begin{aligned} \bar{\mathbf{b}}^{e,trial}_{n+1} &= \bar{\mathbf{F}}_{n+1}\,\bar{\mathbf{b}}^e_n\,\bar{\mathbf{F}}^T_{n+1} \\ \mathbf{s}^{trial}_{n+1} &= \mu\, dev(\bar{\mathbf{b}}^{e,trial}_{n+1}) \end{aligned}$$

3. Compute stresses and plastic entropy:

   Set $\bar{\mu} = \dfrac{\mu}{3}\, tr(\bar{\mathbf{b}}^{e,trial}_{n+1})$

   Set $\mathbf{n}_{n+1} = \dfrac{\mathbf{s}^{trial}_{n+1}}{\|\mathbf{s}^{trial}_{n+1}\|}$ and update:

$$\begin{aligned} \tilde{\mathbf{s}}_{n+1} &= \mathbf{s}^{trial}_{n+1} - 2\,\Delta\tilde{\lambda}_{n+1}\,\bar{\mu}\,\mathbf{n}_{n+1} \\ \tilde{\eta}^{\,p}_{n+1} &= \eta^p_n - \sqrt{\frac{2}{3}}\Delta\tilde{\lambda}_{n+1}\partial_\theta\left(\tilde{\sigma}_{y,n+1} + \beta_{n+1}(\tilde{\bar{e}}^{\,p}_{n+1})\right) \end{aligned}$$

4. Compute plastic power:

$$\tilde{\mathcal{D}}^{n+1}_{mech} = \chi\sqrt{\frac{2}{3}}\left(\tilde{\sigma}_y + \tilde{\beta}\right)_{n+1}\frac{\Delta\tilde{\lambda}_{n+1}}{\Delta t}$$

The definition of the variables that appear in this box are explained in references (Simo and Hughes (1998); Simo (1988a); Simo (1988b))

Box 3. Impl-Ex Explicit integration flowchart for thermo-elastoplastic models.

inelastic and vice versa, but if a time step is small enough as is usually in metal cutting simulations or a time step control is used, this worrying effect does not occur. In Rodriguez et al. (2016), the effect of the time step in the presence of overshoot and oscillations in a thermo-mechanical traction test is studied, it is shown that the effect disappear as the time step is decreased. Now, the values of $\tilde{\mathbf{s}}_{n+1}$, $\tilde{\bar{e}}^{\,p}_{n+1}$ and $\tilde{\eta}^{\,p}_{n+1}$ can be pursued in terms of extrapolated plastic multiplier yielding the Impl-Ex integrated values. The Impl-Ex explicit stage for both cases is summarized in Box 3.

5. Coupled thermo-mechanical contact

Compared to regular initial boundary value problems, special boundary constraints are imposed in contact problems which

govern the interface motion and possible singularities. For classical contact problems the constraints express non-penetration (unilateral) condition, third Newton's law and law of surface friction. The normal contact condition prevents the penetration of one body into another and the tangential slip represents frictional behavior of a contact surface. There are various approaches established for resolving the contact problem. One of these techniques applied for imposing contact conditions in the normal direction is the formulation of non-penetration condition, as a purely geometrical constraint.

In this work we have used two different approaches, in the first one the tool is considered rigid allowing for a simple and robust treatment of the mechanical contact (usually frictionless). In the second approach the tool is considered deformable. The mechanical contact will take into account friction and the treatment of the thermal phenomena occurring at the contact interface.

In both cases contact constraints are implemented based on the penalty approach by imposing the normal springs at the contact interface.

5.1. Rigid tool contact

The first approach to take into account the interaction between a cutter and a workpiece is to consider the tool as a rigid element and the workpiece as deformable body. If the cutter is rigid, the geometry of that element is not going to change during the contact. The best way to describe a fixed geometry is using the mathematical description of its boundary. That allows us to avoid the drawbacks coming from the treatment of contact with a wall of finite elements.

The contact between finite elements require a more complex geometrical contact search and an special master-slave structure. There is usually a lack of continuity from one element to another that comes from the finite element discretization. That fact degradates the convergence of the solution because non-smooth contact forces are obtained from the computation of the constraint in a discrete interface.

The first step for a good definition of the contact forces is a good characterization of the contacting geometry. This will be done using a parametrization of the tool surface. The second step is the mathematical description of the contact constraint. Once an active set of contacts are determined, that constraint is included in the linear momentum balance equation.

5.1.1. Parametrization of the contact tool surface

The geometrical scheme considered to describe a cutting tool can be characterized with three parameters: the tip radius, the angle of the rake face (rake angle) and the angle of the flank face (clearance angle) (see Fig. 4). Defining these three parameters a circle (or a cylinder in 3D) and two planes tangent to that circle are mathematically determined. For the contact detection, one must also define the exterior side of the tool. When a particle of the deformable domain is going to exceed the described contour that particle will be in contact with the tool.

5.1.2. Normal contact with a rigid tool

The definition of the outward normal direction $\mathbf{n}$ will be given by the mathematical equation characterizing the rigid tool surface. Once a particle enters in contact with one of the surfaces the normal gap g_N will be computed projecting the exceeding distance vector into that normal. Using a penalty approach, the constitutive equation for the normal force P_N is given by

$$P_N = \kappa g_N \tag{14}$$

where the κ is the penalty parameter. The contact constraint contribution for the weak form of the linear momentum equation is

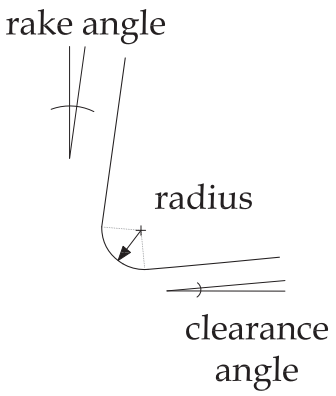

Fig. 4. Rigid tool definition parameters.

given by

$$\int_{\Gamma_{cont}} w_i P_N n_i \, d\Gamma_{cont} = P_N \mathbf{n} \tag{15}$$

The tangential contact can also be considered in the same way as the normal contact. Projecting the particles exceeding distance vector in the tangent direction defined by the rigid surfaces, the tangential gap is determined. Applying a friction law the force magnitude is determined (see Section 5.2.2 for slip conditions) and can be added to the contact constraint.

5.2. Deformable tool contact

In order to extend the contact modeling possibilities the tool must be considered deformable. In this case the interaction is more expensive because both contacting surfaces are susceptible to deform. The contact is governing the interface motion introducing a new non-linearity to the system. The normal contact condition is considered to prevent the penetration of one body into another and for the tangential direction, elastic-plastic constitutive laws will be used to distinguish the sticking and sliding states.

In sticking interfaces, either a geometrical constraint equation, or a constitutive law for the tangential relative micro displacements between the contacting bodies can be applied. For tangential sliding between bodies, a special constitutive equation for friction must be employed.

In this study, a penalty approach is implemented for the tangential case. The stiffness of the tangential spring will be modified according to a regularized Coulomb friction law.

5.2.1. Normal contact

The node-to-segment (NTS) contact element is one of the most commonly used discretization in large deformation simulations of contact problems (de Saracibar, 1998; Wriggers and Simo, 1985). Consider that a workpiece particle s with coordinates $\mathbf{x}_s^{(1)}$ and temperature $\theta_s^{(1)}$ comes into contact with a tool segment (master body) defined by the nodal coordinates $\mathbf{x}_1^{(2)}$, $\mathbf{x}_2^{(2)}$ and nodal temperature $\theta_1^{(2)}$, $\theta_2^{(2)}$ (see Fig. 5). By introducing the surface coordinates along the tool surface, we have

$$\mathbf{x}^{(2)}(\xi) = \mathbf{x}_1^{(2)} + (\mathbf{x}_2^{(2)} - \mathbf{x}_1^{(2)})\xi \tag{16}$$

and

$$\theta^{(2)}(\xi) = \theta_1^{(2)} + (\theta_2^{(2)} - \theta_1^{(2)})\xi \tag{17}$$

where $\mathbf{x}^{(2)}(\xi)$ and $\theta^{(2)}(\xi)$ are the linear interpolation of the master surface and the master temperature surface respectively. The normalized tangent vector of the master segment is computed as

$$\mathbf{a}_1^{(2)} = (\mathbf{x}_2^{(2)} - \mathbf{x}_1^{(2)})/l \tag{18}$$

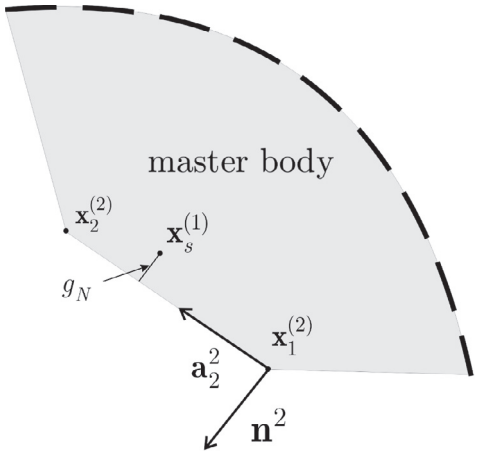

Fig. 5. Node-to-segment contact element.

where $l = \|\mathbf{x}_2^{(2)} - \mathbf{x}_1^{(2)}\|$ is the length of the master segmented. The unit outward normal to the master segment can be computed as

$$\mathbf{n}^{(2)} = \mathbf{e}_3 \times \mathbf{a}_1^{(2)} \tag{19}$$

The normal gap can be written as

$$g_N = \mathbf{x}_1^{(s)} - (1-\bar{\xi})\mathbf{x}_1^{(2)} - \bar{\xi}\mathbf{x}_2^{(2)} \tag{20}$$

where $\bar{\xi}$ is the projection of the workpiece particle $\mathbf{x}_s^{(1)}$ onto the master segment. Mathematically, the projection is written as

$$\bar{\xi} = (\mathbf{x}_1^{(s)} - \mathbf{x}_1^{(2)})\mathbf{a}_1^{(2)}/l \tag{21}$$

Using a penalty approach, the contribution of the thermo-mechanical contact in the discretized mechanical weak form is

$$\mathbf{F}_{\mathbf{u},cont}(\mathbf{u}) = P_N \mathbf{N}_s \tag{22}$$

where P_N is the magnitude of the penalized normal force (see Eq. (14) and the vector $\mathbf{N}_s$ is given by

$$\mathbf{N}_s = \begin{bmatrix} \mathbf{n}_1^{(2)} \\ -(1-\bar{\xi})\mathbf{n}_1^{(2)} \\ -\bar{\xi}\mathbf{n}_1^{(2)} \end{bmatrix} \tag{23}$$

5.2.2. Tangential contact: Friction laws

Let us introduce the discrete relative tangential velocity

$$\dot{g}_T = (\bar{\xi} - \bar{\xi}_0)l/\Delta t \tag{24}$$

and the discrete relative tangent displacement

$$g_T = (\bar{\xi} - \bar{\xi}_0)l \tag{25}$$

where $\bar{\xi}_0$ is the projection of the slave node on the master surface at the beginning of the time step.

The friction force is modeled using a regularized Coulomb friction law as follows

$$P_T = \mu P_N \tanh\left(\frac{\dot{g}_T}{V_{ref}}\right) \tag{26}$$

where μ is the friction coefficient between the workpiece and the tool and V_{ref} is a regularization parameter. As V_{ref} tends to 0 the regularized friction law tends to the Coulomb friction Law. In the simulation presented in this work, a value of 1mm/s has been used. The contribution of the friction force to the balance of momentum take the form

$$\mathbf{F}_{\mathbf{u},cont}(\mathbf{u}) = P_T \mathbf{T}_s \tag{27}$$

where the vector $\mathbf{T}_s$ is given by

$$\mathbf{T}_s = \begin{bmatrix} \mathbf{a}_1^{(2)} \\ -(1-\bar{\xi})\mathbf{a}_1^{(2)} \\ -\bar{\xi}\mathbf{a}_1^{(2)} \end{bmatrix} \tag{28}$$

The solution of the balance of momentum equation using Newton's method need the linearization of the normal and tangential contact forces, to see the derivation of this matrices (see Rodriguez et al. (2015)).

5.2.3. Heat transfer at the contact interface

The heart flux at the contact zone needs a constitutive equation for its determination. We assume the following structure for the constitutive equation of the heat flux

$$Q = h g_T \tag{29}$$

where

$$g_T = (\theta_s^{(1)} - (1-\bar{\xi})\theta_1^{(2)} - \bar{\xi}\theta_2^{(2)}) \tag{30}$$

where h is the thermal conductance coefficient. The heat flux Q models at the tool-chip interface the heat conduction through spots, heat conduction trough the gas contained cavities and radiation between micro-cavities surfaces. As a result, the heat transfer coefficient h is usually assumed to depend on contact pressure and temperature. In this work, we assume the heat transfer coefficient constant.

The contribution to the balance of energy due to conduction, convection and radiation is given bay

$$\mathbf{F}_{\theta,cont}(\theta) = Q\boldsymbol{\Theta}_Q \tag{31}$$

where the vector $\mathbf{T}_s$ is given by

$$\boldsymbol{\Theta}_Q = \begin{bmatrix} 1 \\ -(1-\bar{\xi}) \\ -\bar{\xi} \end{bmatrix} \tag{32}$$

When two bodies, say a tool and a workpiece, are in contact, the rate at which heat is generated due to friction is shared between both bodies. In this work, we suppose that the half the heat is entering the tool and half is entering to the workpiece. For more sophisticated models of the heat partition due to friction (see Sekhon and Chenot (1993)). The heat generated due to friction using a regularized Coulomb friction law is given by the following expression

$$D_{fric} = P_T \dot{g}_T = \mu \left| P_N \tanh\left(\frac{\dot{g}_T}{V_{ref}}\right)\dot{g}_T \right| \tag{33}$$

The contribution of the heat generation to the balance of energy take the form

$$\mathbf{F}_{\theta,cont}(\theta) = D_{fric}\boldsymbol{\Theta}_s \tag{34}$$

where the vector $\mathbf{T}_s$ is given by

$$\boldsymbol{\Theta}_s = \begin{bmatrix} 1/2 \\ -1/2(1-\bar{\xi}) \\ -1/2\bar{\xi} \end{bmatrix} \tag{35}$$

6. Integration of the IBVP using IMPL-EX

The usual way to solve the thermo-mechanical problem is to decouple it in two simpler problems. The isothermal scheme presented in Simo and Miehe (1992) decouples the thermo-mechanical problem in two simple problems, but, yet, the mechanical problem is coupled with the evolution equations of the internal variables and the thermal problem is also coupled. The evolution equations of the internal variables, both of them are coupled

INTEGRATION OF THE IBVP / IMPL-EX SPLIT

1. CONTACT SEARCH

   Search for the *Active Set* of Contacts with a Rigid Tool or with a Deformable Tool

2. MECHANICAL SOLUTION (for a fixed initial temperature)

   (i) ISOTHERMAL ELASTOPLASTIC PROBLEM

   (primary variables $\mathbf{u}_{n+1}, \mathbf{p}_{n+1}$ and internal variables $\mathbf{b}^e_n, \bar{\mathbf{e}}^{\,p}_n, \eta^p_n$)

   - ITERATIVE LOOP

     (a) IMPL-**EX** $\quad \mathbf{b}^e_n, \bar{\mathbf{e}}^{\,p}_n, \eta^p_n \;\rightarrow\; \text{(Box 3)} \;\rightarrow\; \tilde{\mathbf{b}}^e_n, \tilde{\bar{e}}^p_{n+1}, \tilde{\eta}^{\,p}_n$

     (b) Momentum equation (with the contact constraint)

     $$\nabla \cdot (dev(\boldsymbol{\sigma}) + p\mathbb{1}) + \mathbf{b} - \rho\dot{\mathbf{v}} = 0 \tag{36}$$

     (c) Pressure balance equation (with PPP stabilization S_{PPP})

     $$p - (\frac{1}{3}\mathbb{1} : \boldsymbol{\sigma}) + S_{\text{PPP}} = 0 \tag{37}$$

     (d) Update the *Active Set* of Contacts

   - CONVERGENCE ACHIEVED
   $$\begin{aligned} \mathbf{v}_{n+1} &= \mathbf{v}_n + \dot{\mathbf{v}}_{n+1}\Delta t \\ \mathbf{u}_{n+1} &= \mathbf{u}_n + \mathbf{v}_{n+1}\Delta t \\ \mathbf{p}_{n+1} &= \mathbf{p}_n + \Delta\mathbf{p}_{n+1} \end{aligned}$$

3. THERMAL SOLUTION (for a fixed configuration)

   (ii) THERMOPLASTIC PROBLEM

   (primary variable θ_{n+1} and internal variables $\mathbf{b}^e_n, \bar{\mathbf{e}}^{\,p}_n, \eta^p_n$) 2mm

   - ITERATIVE LOOP

     (a) IMPL-**EX** $\quad \mathbf{b}^e_n, \bar{\mathbf{e}}^{\,p}_n, \eta^p_n \;\rightarrow\; \text{(Box 3)} \;\rightarrow\; \tilde{\tilde{\mathbf{b}}}^e_{n+1}, \tilde{\tilde{\bar{e}}}^p_{n+1}, \tilde{\tilde{\eta}}^p_{n+1}$

     (b) Energy equation (with the contact constraint)

     $$\dot{e} + \nabla \cdot (\mathbf{q}) - \mathcal{D}_{int} = 0 \tag{38}$$

   - CONVERGENCE ACHIEVED $\quad \theta_{n+1} = \theta_n + \dot{\theta}_{n+1}\Delta t$

4. **IMPL**-EX (Implicit backward-Euler integration of the Plasticity law)

$$\tilde{\tilde{\mathbf{b}}}^e_{n+1}, \tilde{\tilde{\bar{e}}}_{n+1}, \tilde{\tilde{\eta}}^p_{n+1} = f\left((\mathbf{u}_{n+1}, \theta_{n+1}), (\mathbf{b}^e_{n+1}, \bar{\mathbf{e}}_{n+1}, \eta_{n+1})\right)$$

The definition of the variables that appear in this box are explained in section 3 and references [45, 39].

Box 4. Isothermal IMPL-EX split.

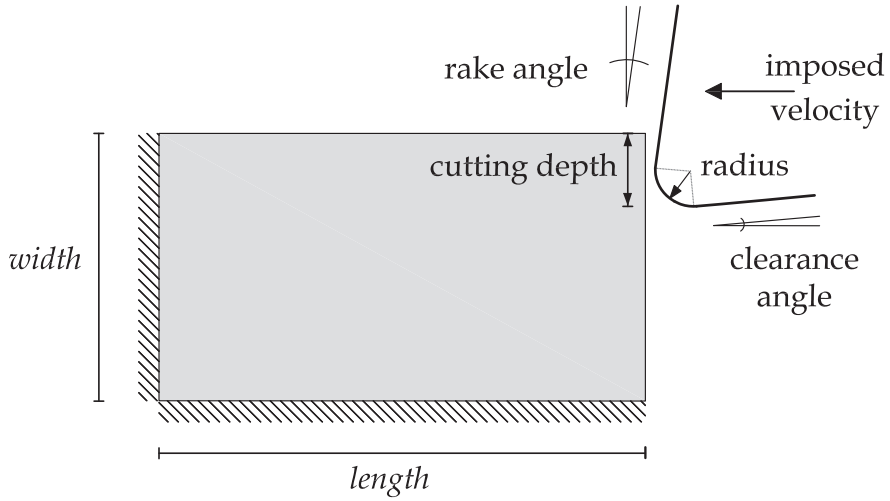

Fig. 6. Linear cutting test model.

through the plastic multiplier. The above reason, suggests decoupling the problem in the following three simple problems: (i) an elastic problem with shear modulus changing from element to element, (ii) a thermal problem with a temperature dependent plastic heat source and (iii) a relaxation process affecting the stress and the internal variables at the integration points.

In this section, we present a new staggered algorithm for the solution of the IBVP, which is based on the isothermal split presented in Simo and Miehe (1992) and the IMPL-EX integration scheme of the constitutive equations presented in Oliver et al. (2008). Using the ingredients presented above, the solution of the coupled system of ODE (37), (36) and (38) could be decoupled in the three simple problems mentioned previously. In addition, the elastic and the thermal problems update the internal variables according to a predicted plastic multiplier (explicit), while the constitutive equations keep the displacements, velocities and temperatures unchanged (implicit).

For simplicity, a partition of the time domain $I := [0, T]$ into N time steps, of the same length Δt is considered. Let us focus on the time step $t_n \to t_{n+1}$, where $\Delta t = t_{n+1} - t_n$. An implicit backward-Euler difference scheme is applied to the momentum equation and to the energy equation. In the first step the extrapolation of the plastic multiplier $\Delta\lambda_{n+1} = \Delta\lambda_n$ is done. Consequently, the stresses $\boldsymbol{\sigma}_{n+1}$ are computed via in IMPL-EX integration scheme of the constitutive equation. After that, the balance of momentum (4) is solved implicitly providing the nodal displacement and pressure for fixed initial temperature. The balance of momentum equations, providing a fixed initial temperature and an extrapolated value of the internal variables, constitutes a non-linear system to solve. In this case, the non-linearity of the system appears due to the geometrical part of the linearized equations. Therefore they have to be iteratively solved until convergence is achieved.

The solution of the balance of momentum equation for a fixed initial temperature gives an update of the primary variables $\mathbf{u}_{n+1}, \mathbf{p}_{n+1}$ and a first update of the internal variables. Then, in the second step, the solution of the balance of energy with initial conditions $\mathbf{u}_{n+1}, \mathbf{p}_{n+1}, \theta_n$, initial internal variables $\mathbf{b}^e_n, \bar{\mathbf{e}}^p_n, \eta^p_n$ and the extrapolation of the plastic multiplier $\Delta\lambda_{n+1} = \Delta\lambda_n$ gives an update of the primary variable θ_{n+1} and a second update of the internal plastic variables (at fixed configuration). Finally, in the third step, the values of $\mathbf{u}_{n+1}, \mathbf{p}_{n+1}, \theta_{n+1}$ remain fixed, and an implicit backward-Euler integration of the constitutive model (Simo and Miehe (1992)) is done using as initial internal variables $\mathbf{b}^e_n, \bar{\mathbf{e}}^p_n, \eta^p_n$. The set of internal variables obtained at the end of this time step, will be the set of internal variables used as the starting point in the next step of the fractional step method proposed in this work. The explained flowchart about the isothermal IMPL-EX split is shown in Box 4.

It is interesting to note that the boundary values of the momentum equation are included in the elastic equations with shear modulus changing from element to element and the boundary values of the balance of energy are imposed on the thermal problem with temperature dependent plastic heat source. In addition, the plasticity law integration consists on solving a collection of systems of ordinary differential equations, each one of them belonging to a different integration point. A full Newton–Raphson scheme is used for the solution of the non-linear systems.

7. Examples

In next section different examples are presented concerning to the simulation of linear cutting tests. Each one of them has a particular set of cutting properties and material models. Fig. 6 shows the general scheme for the model of a linear cutting test example. In each case the proper numerical techniques have been applied in order to reproduce the continuous cut. We start with two examples where the tool is rigid, the contact is frictionless and the constitutive model is changed from a rate-independent to a rate-dependent plasticity law. We change also the angle of the tool to detect its influence in the analysis results.

In the next cases, a rate-dependent law and a deformable tool is considered. In the first one, the heat transfer between the workpiece and the tool is neglected and the contact is considered frictionless. After analyzing the influence of the introduced changes on the results we study a second example. In this one the friction and the transfer of heat between the tool and the workpiece is considered. The heat produced in the contact interface by the friction of materials is also taken into account.

7.1. Linear cutting test with a frictionless rigid tool rate independent law

Our first application concerns the cutting of a rectangular block of a common steel of length 7 mm and width 3.6 mm at a velocity of 3.33 m/s, a cutting depth of 0.10 mm, a rake angle of 0°, a clearance angle of 5° and a tool radius of 0.025 mm. Material behavior is given by a *Voce* law 4.3.1 that takes into account thermal softening (see Table 1). Conductivity and specific heat does not depend on temperature, we consider them constant. The following

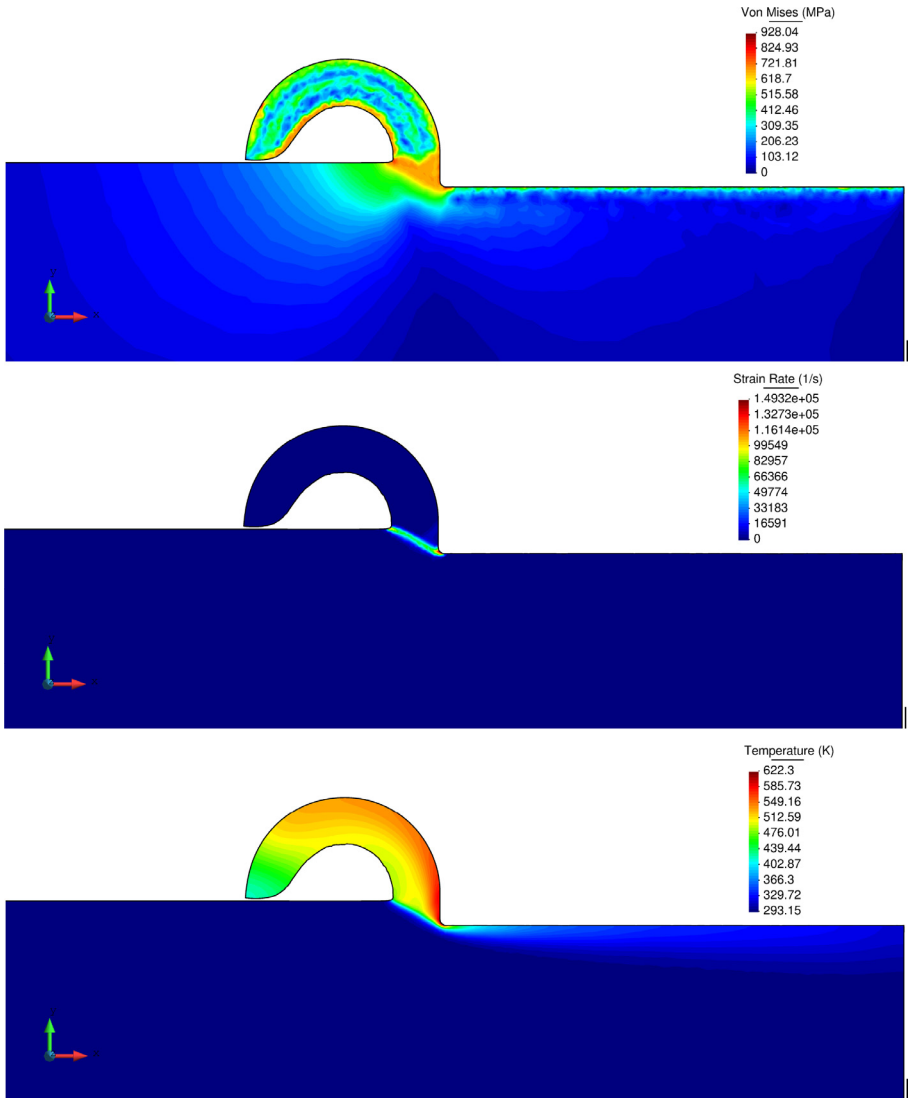

Fig. 7. Continuous chip formation using a rate independent yield function: (a) *von Mises* (MPa) ; (b) strain rate(1/s); (c) temperature(K).

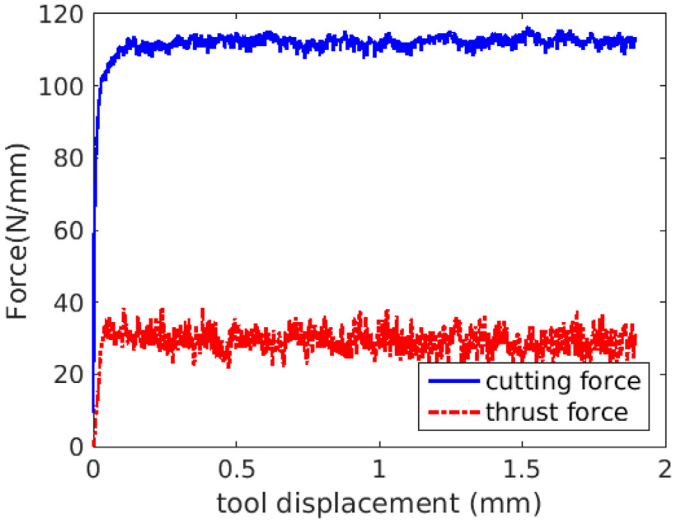

Fig. 8. Cutting and thrust force versus cutting tool displacement for a rate independent yield function.

Table 1
Rate independent yield function. Material properties.

Young Modulus	E	$206.9 \cdot 10^3$	MPa
Poisson Ratio	ν	0.3	
Density	ρ	$7.8 \cdot 10^{-9}$	Ns^2/mm^4
Yield Stress	σ_y	450	MPa
Saturation Hardening	K_{inf}	715	MPa
Linear Hardening	H	129.24	MPa
Hardening Exponent	δ	16.93	
Expansion Coefficient	α	$1 \cdot 10^{-5}$	K^{-1}
Thermal Capacity	c	$0.46 \cdot 10^9$	mm^2/s^2K
Thermal Conductivity	k	45	N/sK
Flow Stress Softening	w_0	0.001	K^{-1}
Hardening Softening	w_h	0.001	K^{-1}
Dissipation Factor	χ	0.9	
Reference Temperature	θ_0	293.15	K

assumptions are made for the tool-contact: the tool is supposed to be rigid and friction is neglected. Furthermore, the thermal exchange between the block and the tool are also neglected. The inertia of the block is neglected. Implicit dynamics is used. Time steps were of $1.041 \cdot 10^{-7}$ s which it takes approximately $5.7 \cdot 10^3$ steps for a tool travel of 1.89 mm. The number of particles used

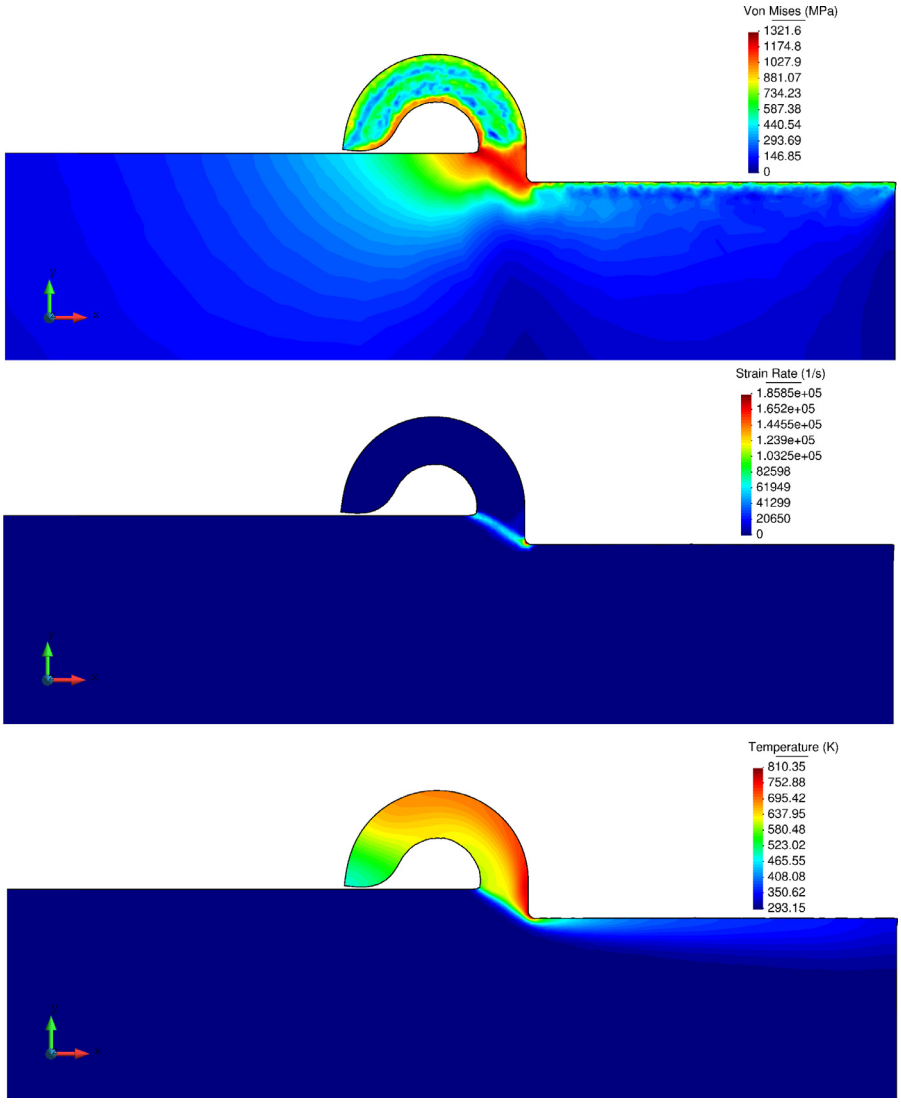

Fig. 9. Continuous chip formation using a rate independent yield function: (a) *von Mises* (MPa) ; (b) strain rate(1/s); (c) temperature(K).

to discretize the workpiece was between 6541 and 8352. The assumption that the tool is rigid is reasonable, since the deformation of the tool is secondary relatively to the excessive plastic deformation of the workpiece.

Temperature, effective plastic strain rate and *von Mises* contours are presented in Fig. 7. *von Mises* stress, shown in Fig. 7, demonstrates that relatively high stresses arise in the primary shear zone and at the tool chip interface. The localization of this zone agrees with simplified models, but it differs in that the maximum stress is not confined to only a plane of excessive shear. It is also important to note the development of residual stresses at and below the surface of the produced new surface and in the upper part of the chip, especially near the tool-chip interface where unloading due to curling of the chip occurred. The effective strain rate in the primary and the secondary shear zone is of the order of $10 \cdot 10^5\,s^{-1}$ and has its highest value close to the tool tip.

Finally, in Fig. 7, the temperature distribution is shown in the workpiece. The temperature reaches its peak in the incident at the tip of the tool on the machined surface. Fig. 8 depicts cutting and thrust forces applied on the tool, obtained from the simulation. The cutting and thrust forces reach a steady state as expected in continuous chip formation.

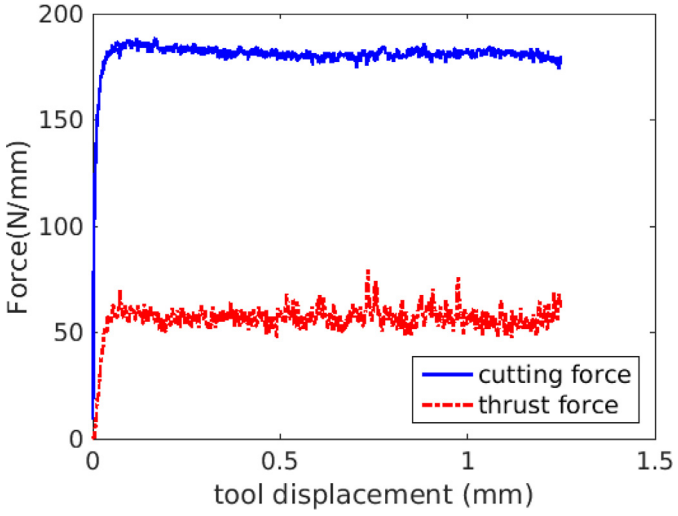

Fig. 10. Cutting and thrust force versus cutting tool displacement for a rate independent yield function.

The contact length between the tool and the workpiece, the deformed chip thickness, and the shear angle are 0.16 mm, 0.25 mm and 22 °, respectively.

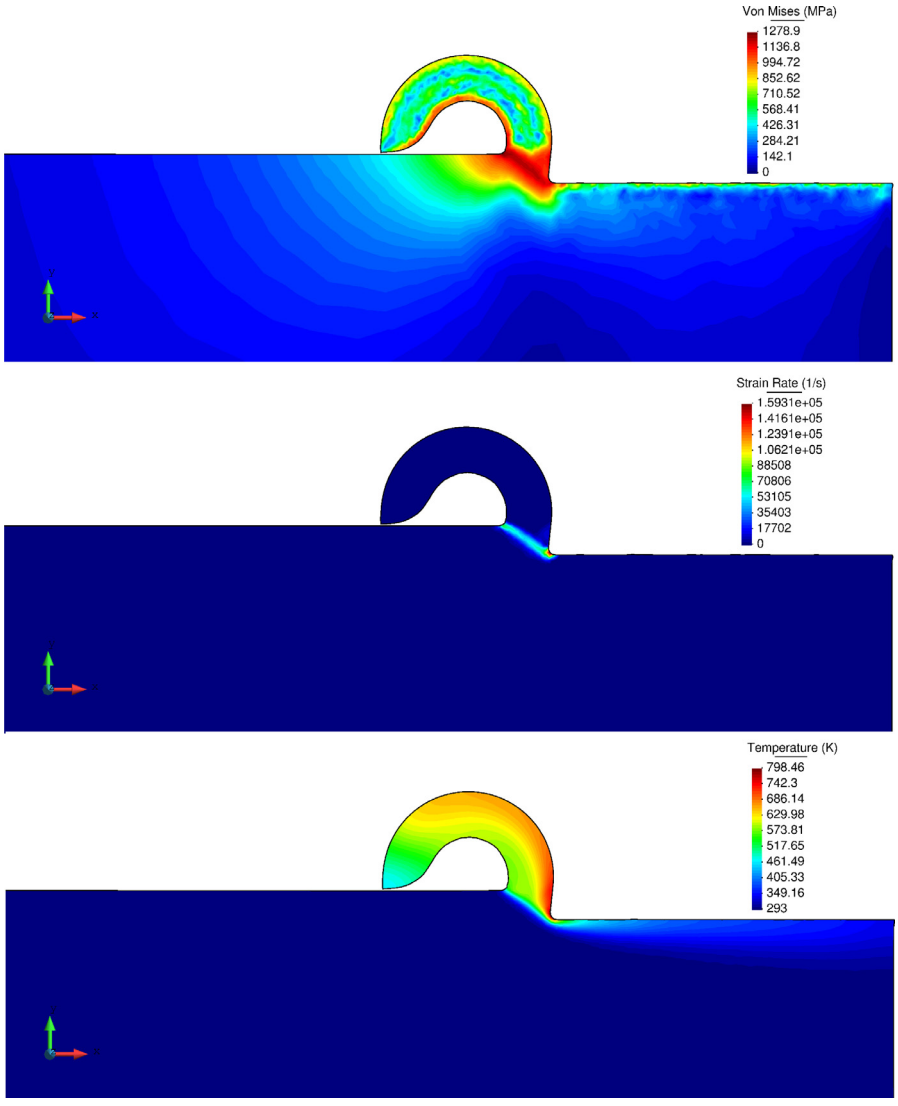

Fig. 11. Continuous chip formation with a rigid tool using a rake angle of 6°: (a) *von Mises* (MPa) ; (b) strain rate(1/s); (c) temperature(K).

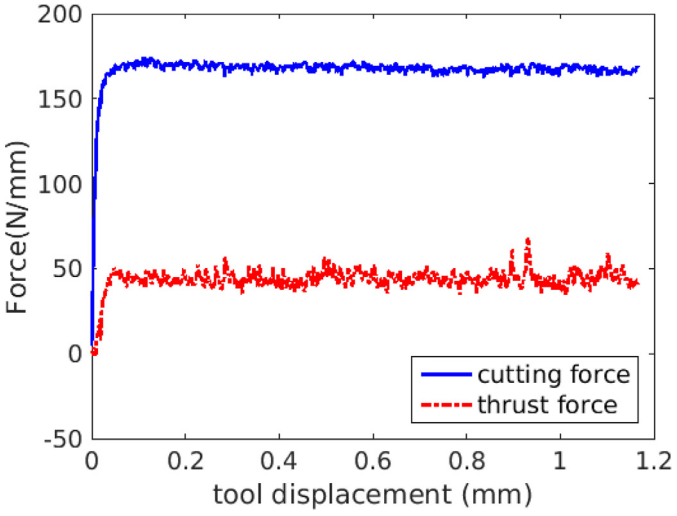

Fig. 12. Cutting and thrust force versus cutting tool displacement using a rake angle of 6°.

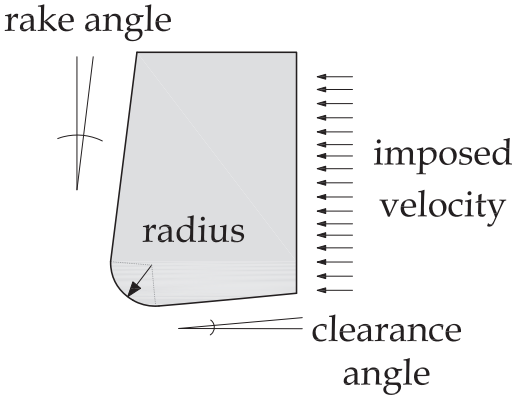

Fig. 13. Deformable tool model parameters.

7.2. Linear cutting test with a frictionless rigid tool and a rate dependent law

The second application concerns the cutting of a rectangular block of high strength AISI 4340 steel of length 7 mm and width 3.6 mm, at a velocity of 3.33 m/s, a cutting depth of 0.1 mm, a clearance angle of 5°, a rake angle of 0° and a tool radius of 0.025 mm.

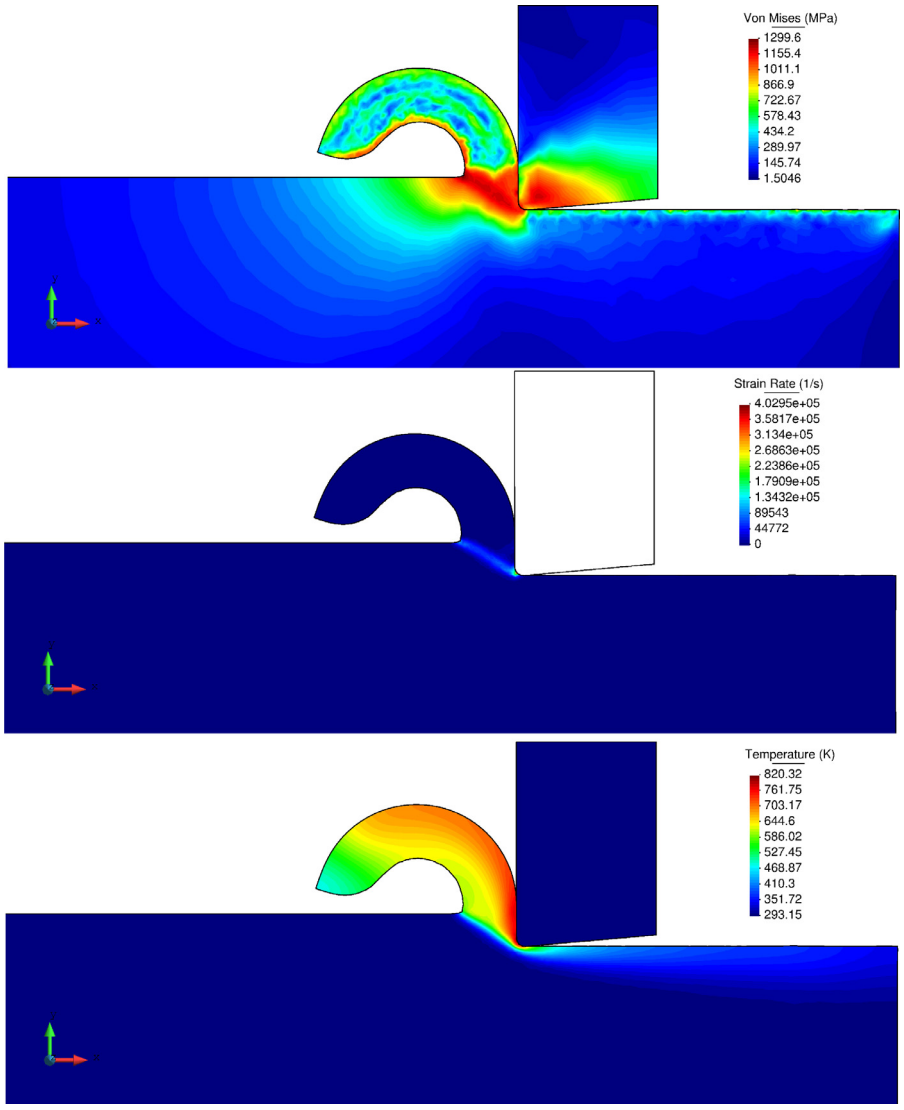

Fig. 14. Continuous chip formation with a deformable tool using a rake angle of 0°: (a) *von Mises* (MPa) ; (b) strain rate(1/s); (c) temperature(K).

Table 2
Rate dependent yield function. AISI 4340 steel properties.

Young Modulus	E	$200.5 \cdot 10^3$	MPa
Poisson Ratio	ν	0.3	
Density	ρ	$7.844 \cdot 10^{-9}$	Ns^2/mm^4
Johnson's Cook A constant	A	792	MPa
Johnson's Cook B constant	B	510	MPa
Johnson's Cook C constant	C	0.014	
Johnson's Cook n constant	n	0.26	
Johnson's Cook m constant	m	1.03	
Thermal Capacity	c	$0.46 \cdot 10^9$	mm^2/s^2K
Thermal Conductivity	k	50	N/sK
Expansion Coefficient	α	$1 \cdot 10^{-5}$	K^{-1}
Reference Temperature	θ_0	293.15	K

Material behavior is given by a *Johnson Cook* law that takes into account thermal softening and strain rate hardening Table 2. Conductivity and specific heat does not depend on temperature, we consider them constant. The following assumptions are made: the tool is supposed to be rigid and friction is neglected. Furthermore, the thermal exchange between the block and the tool are also neglected. The inertia of the block is neglected. Implicit dynamics is used. Time steps were of $1.041 \cdot 10^{-7}$ s which takes $3.6 \cdot 10^3$ steps for a tool travel of 1.24 mm.As described, the example has essentially the same parameters as the previous one excluding the rate dependent yield function. The number of particles used to discretize the workpiece was between 6531 and 7806. Only insertion of particles was used for this example.

Looking at the results, the deformation is largely confined to the primary shear zone and to the boundary layer adjacent to the tool Fig. 9. No shear localization occurs and a continuous chip formation is predicted. A typical distribution of temperature field within the workpiece material is shown in Fig. 9. Highest temperatures are observed on the outside surface of the chip currently in contact with the rake face. Temperature in the direction of the shear plane is found to vary from high of about 810 K near the cutting edge to about 510 K near the unmachined free surface. Also temperature along the rake face changes from 810 K near the cutting edge to 760 K at the point where the contact between the tool and the chip come to an end.

7.2.1. Linear cutting test changing the angle of the rigid tool

In this example the previous simulation is modeled changing only the rigid tool geometry. The change is only applied in the rake angle which is considered, in this case, of 6°. The number of particles used to discretize the workpiece was between 6529 and 7682. The material behavior of the workpiece is described by a

Johnson Cook law taking into account thermal softening and strain rate hardening, and using the parameters of Table 2.

In this case, deformation is largely confined to the primary shear zone and to the boundary layer adjacent to the tool Fig. 11, as occurred in the other examples. No shear localization occurs and a continuous chip formation is predicted. A typical distribution of temperature field within the workpiece material is shown in Fig. 11. Highest temperatures are observed at the outside surface of the chip currently in contact with the rake face. Temperature in the direction of the shear plane varies from 790 K near the cutting edge to about 500 K near the unmachined free surface. Also temperature along the rake face changes from 790 K near the cutting edge to 750 K at the point where the contact between the tool and the chip comes to an end.

The largest accumulated plastic strains occur within the boundary layer adjacent to the tool. In this region, the flow of the material is facilitated by thermal softening and the plastic strains attain values up to 4. Strains in the interior of the chip remain between 1 to 1.5 upon exit from the primary shear zone. Fig. 12 shows the horizontal and vertical predicted cutting forces. It is found that horizontal cutting force rise quickly to a value of 170 N per mm of width of cut within a short distance of 0.05 mm. Then as the chip thickness and the cutting temperatures in the deforming zone stabilize, the horizontal cutting force holds to this constant value of 170 N per mm width of cut. The steady state vertical force component, also known as thrust force was found to average around 48, N per mm width of cut. The contact length between the tool and the workpiece, the deformed chip thickness and the shear angle are 0.15 mm, 0.16 mm and 30°, respectively.

7.3. Linear cutting test with a frictionless deformable tool and a rate dependent law

The next example concerns the cutting of a rectangular block of high strength AISI 4340 steel modeled using the Johnson-Cook hardening law with the tool considered as a deformable body. From now on, the deformable contact will be considered increasing the complexity of the contact interaction in each one of the examples. In the former one the hypothesis considered is the closest to the rigid tool cases (frictionless without heat transfer).

The tool has a clearance angle of 5°, a rake angle of 0° and a tool radius of 0.025 mm. The friction and the thermal exchange between the workpiece and the tool are neglected. The materials and processes parameters are collected in Table 2. Conductivity and specific heat of the workpiece and the tool do not depend on temperature, we consider them constant. Workpiece dimensions were taken as 7.0 mm (length) 3.6 mm (depth). Cutting speed was 3.33 m/s and the deep of cut was 0.1 mm. The deformable tool geometry is depicted in Fig. 13.

Each time increment was designed to correspond to a tool travel of $3.47218 \cdot 10^{-4}$ mm. Simulation was continued until the chip comes into contact with the tool. Actually a tool travel of 1.166 mm was covered in $3.360 \cdot 10^{3}$ implicit increments. The number of particles used to discretize the workpiece was between 7957 and 9105.

Fig. 14 shows the contours of equivalent plastic strain rate and the contours of equivalent *von Mises* stress. It is observed that the maximum values of equivalent plastic strain rate and *von Mises* stress occur near the cutting edge and are of the order of $2.58 \cdot 10^{5}\ s^{-1}$ and 1080 MPa respectively.

In Fig. 15 a comparison between the predicted forces using a deformable and a rigid tool is shown, it can be observed that the obtained cutting and feed forces are close to be the same in both cases. Nevertheless, according to our testing experience, if the mesh size and the time step are smaller a slightly lower cutting force and slightly higher feed force is obtained when the deformable tool is used, although a specific study is necessary to probe the last sentence. This occurs due to the change in the local cutting edge geometry (see Rodriguez et al. (2015)).

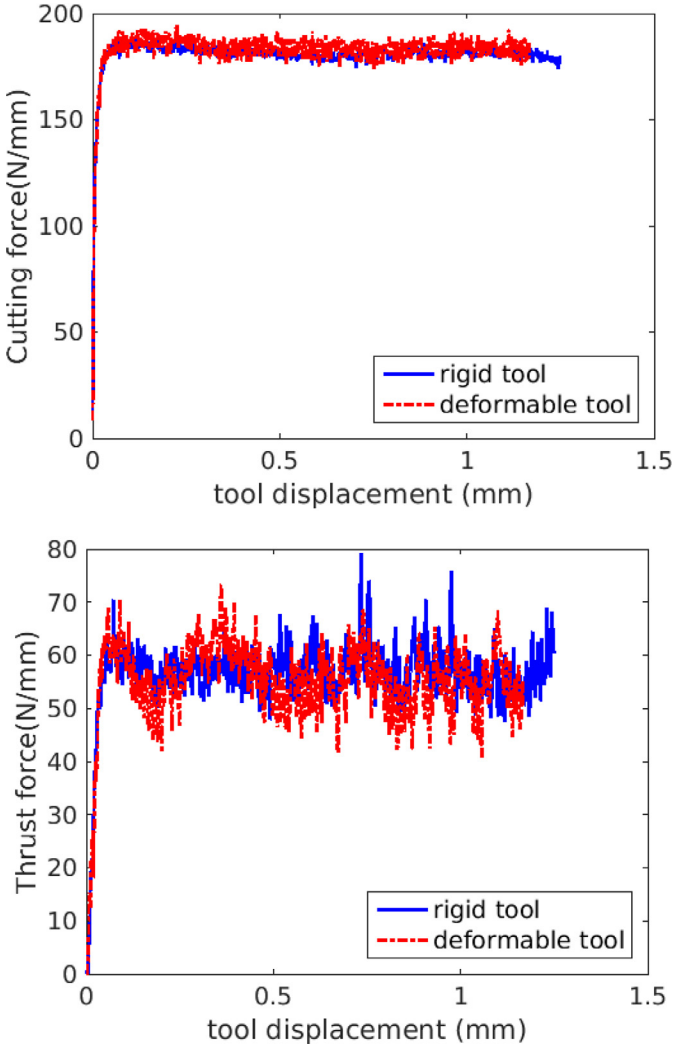

Fig. 15. Cutting and feed forces. A rigid vs. a deformable tool.

The contact length between the tool and the workpiece, the deformed chip thickness and the shear angle are 0.16 mm, 0.14 mm and 30°, respectively. The modelling the deformation of the tool is relevant for example for tool industries, because they want to know where and how failure take place, and one relevant indicator for that is the place where the maximum von Mises stress takes place in the tool.

7.4. Linear cutting test with a deformable tool and a rate dependent law considering friction and heat transfer

In this example, orthogonal dry machining of AISI 4340 steel by a high strength steel tool has been simulated. The cutting is performed at a speed of 3.33 m/s, at a feed of 0.1 mm, a rake angle of 0° and a clearance angle of 5°. The friction at the tool-chip interface is modeled using a regularized *Coulomb* friction law presented in Section 5.2.2 with frictional coefficient $\mu = 0.2$. The mechanical and thermal properties of the workpiece and the tool are the same that were used in previous example. The number of particles used to discretize the workpiece was between 7957 and 9084.

The thermal properties of the tool are supposed to be matched to those of the workpiece, giving an equal portion of frictional heat

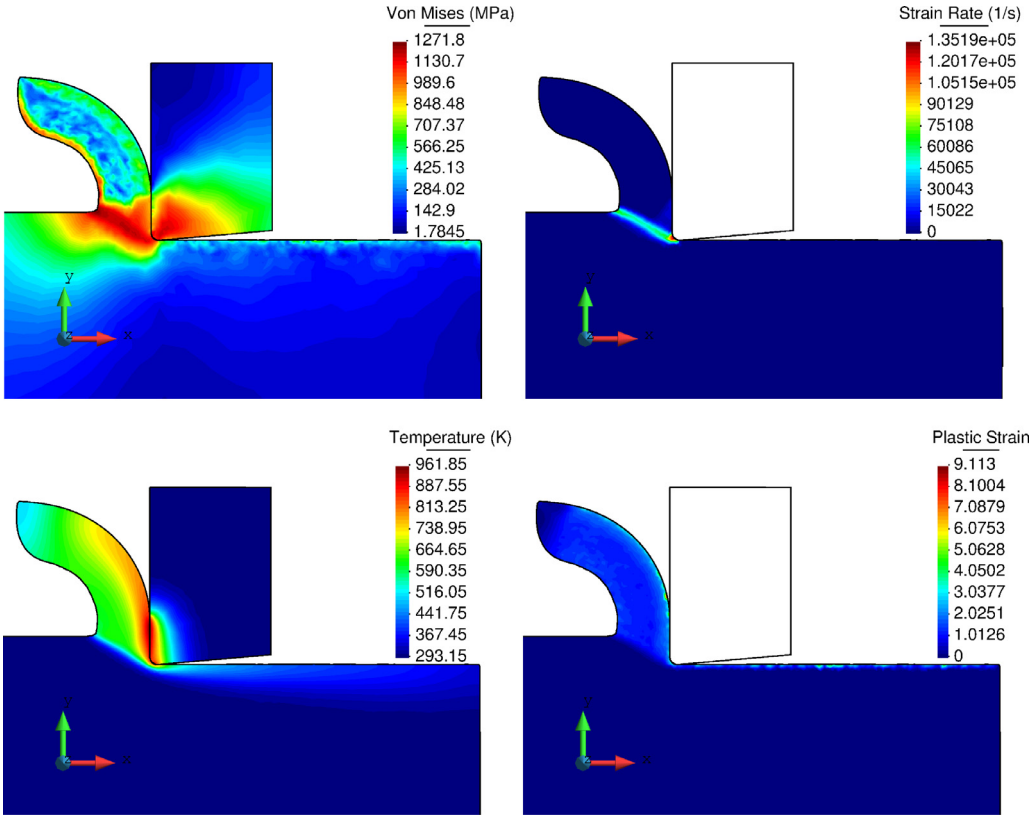

Fig. 16. Continuous chip formation: Deformable tool, friction and heat transfer at the tool chip interface.

allowed for the tool and the chip. The thermal conductance coefficient used was $1e9$ W/m^{2}K, in order to ensure that the thermal gap at the tool-chip interface will be negligible.

Fig. 16 shows the results for the strain rate contours. Strains are concentrated, as expected, near the shear plane and along the rake face. The strain rate reaches $1.35 \cdot 10^5$ s^{-1} in front of the cutting edge.

The temperature field in the tool and the workpiece is also depicted in Fig. 16. The maximum temperature is 961 K and takes place along the rake face. In the same figure, the plastic-strain distribution reaches extremely high values, in some points of the analysis they are close to 14. The *von Mises* stress distribution is also shown in Fig. 16, the maximum stress appears in the tool, close to the cutting edge. In the workpiece, the magnitude of the stress rises in the deformation zone because of the material hardening, but it is limited to 1250 MPa by thermal softening.

The contact length between the tool and the workpiece, the deformed chip thickness and the shear angle are 0.19 mm, 0.18 mm and 29 °, respectively.

A comparison with the frictionless case of the previous example (7.3) is presented in Fig. 17. The comparison shows that the cutting force increases 40 N/mm while the thrust force increases 26 N/mm if friction is considered. Similarly, the contact length and the undeformed chip thickness increase with friction. The reason for these increases cater to the fact that friction hinders the rotational movement of the chip during the cut.

7.5. Validation and competitiveness

In order to validate PFEM strategy with a test case, a cutting process of 42CD4 steel at 300 m/min, with a tool radius of 0.04 mm, a rake angle of 6 ° and a cutting depth of 0.2 mm is proposed. Materials and contact properties used are the same presented in Arrazola (2003). A summary of all the input parameters are found in Tables 3, 4 and 5.

Table 3
Rate dependent yield function. 42CD4 steel properties.

Young Modulus	-	E	$210 \cdot 10^3$	MPa
Poisson Ratio	-	ν	0.3	
Density	-	ρ	$7.844 \cdot 10^{-9}$	Ns^2/mm^4
Johnson's Cook A constant	-	A	598	MPa
Johnson's Cook B constant	-	B	768	MPa
Johnson's Cook C constant	-	C	0.0137	
Johnson's Cook n constant	-	n	0.2092	
Johnson's Cook m constant	-	m	0.807	
Dissipation Factor	-	χ	0.9	
Thermal Capacity	(423–473 K)	c	$0.473 \cdot 10^9$	mm^2/s^2K
	(623–673 K)		$0.519 \cdot 10^9$	mm^2/s^2K
	(823–873 K)		$0.561 \cdot 10^9$	mm^2/s^2K
Thermal Conductivity	(373 K)	k	42.6	N/sK
	(473 K)		42.3	N/sK
	(673 K)		37.7	N/sK
	(873 K)		33.1	N/sK
Expansion Coefficient	(293 K)	α	0.0	K^{-1}
	(673 K)		$1.45 \cdot 10^{-5}$	K^{-1}
Fusion Temperature	-	θ_f	1793	K
Reference Temperature	-	θ_0	293.15	K

The time step used during the simulation was $1.1 \cdot 10^{-8}$ s, as a result 20000 time steps were needed for a tool displacement of 1 mm. At the beginning of the cutting process the workpiece was discretized with 422 particles, due to the insertion of the particles the maximum number reached was 11386.

Fig. 18 shows the temperature field after a cutting length of 1 mm. The maximum tool temperature reached is about 1186 K. It is located far from the cutting edge, and approximately at a distance of 1.25 times the undeformed chip thickness. The maximum *von Mises* stress inside the chip-piece takes place in the primary

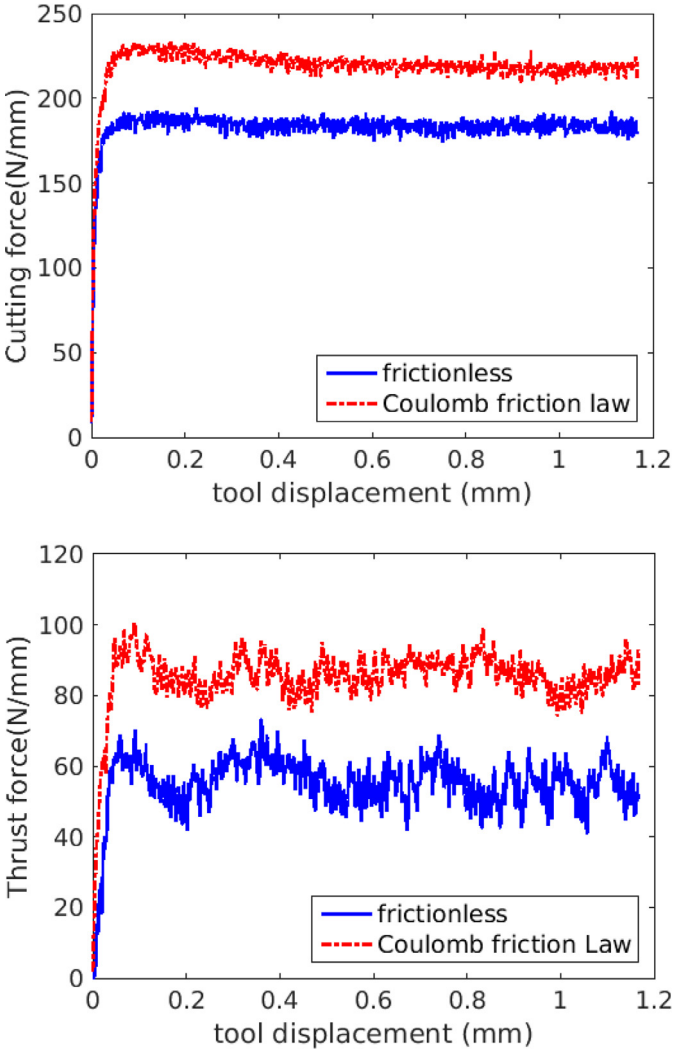

Fig. 17. Cutting and thrust forces: Deformable tool with and without friction. In the case of friction, heat generation and transfer at the tool chip interface is considered.

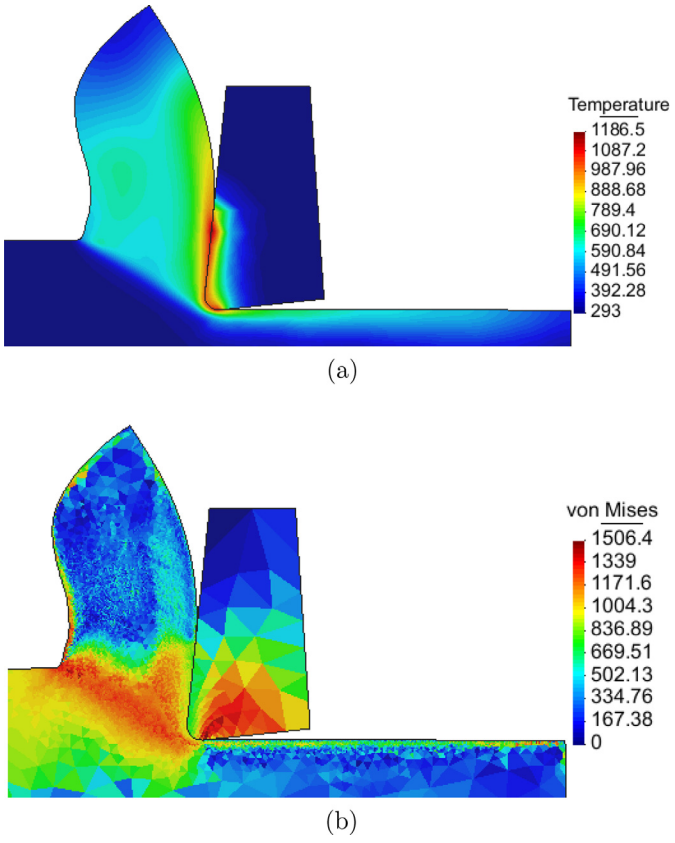

Fig. 18. Orthogonal cutting of 42CD4 steel.

Table 4
Tool 42CD4 steel properties.

Young Modulus	-	E	$210 \cdot 10^3$	MPa
Poisson Ratio	-	ν	0.3	
Density	-	ρ	$7.844 \cdot 10^{-9}$	Ns^2/mm^4
Dissipation Factor	-	χ	0.9	
Thermal Capacity	-	c	$0.20 \cdot 10^9$	mm^2/s^2K
Thermal Conductivity	-	k	25	N/sK
Expansion Coefficient	(293 K)	α	0.0	K^{-1}
	(673 K)		$1.45 \cdot 10^{-5}$	K^{-1}
Fusion Temperature	-	θ_f	1793	K
Reference Temperature	-	θ_0	293.15	K

Table 5
Contact properties.

Thermal Conductance	$1.0 \cdot 10^8$	W/m^2K
Partition Coefficient	0.5	
Friction Coefficient	0.23	
Norton Hoff Coefficient	$6.0 \cdot 10^{-5}$	
Friction Dissipation Factor	1.0	

Table 6
Experimental and numerical results (PFEM).

	Chip thickness (mm)	Cutting force (N)	Feed force (N)	Contact length (mm)
PFEM	0.35	383	105	0.26
Experimental	0.32	395	170	0.49

shear zone, while the maximum *von Mises* inside the tool is close to the point where the tool loses the contact with the machined surface.

Data about experimental results have been obtained from data reported in the literature (Arrazola, 2003). Table 6 compares the numerical and the experimental results obtained for the example presented in this section. It is observed a good agreement between the experimental and the numerical cutting forces however there are large differences between experimental and numerical feed forces. Regarding the chip thickness a relatively good agreement was found between experiments and numerical simulations. Looking at the same table (Table 6), the tool-chip contact length measured in the experiments is about two times greater than the length predicted by the numerical simulations. The differences between the numerical and the experimental results come from two sources: 1) the experiments used to calibrate the Johnson-Cook law are carried out at strain rates lower than the strain rates obtained in machining process and 2) the friction modeling at the tool shape does not follow the Coulomb law (see Svoboda et al. (2010); Arrazola et al. (2008); Filice et al. (2006); Özel (2006). Arrazola et al. (2008), report that the main differences observed between FEM results and experimental ones are the feed force and the tool-chip contact length, where differences of more that 50% can be found for those variables when comparing FEM results with the experimental ones. According to Arrazola et al. (2008) the mismatch in feed force between experimental and numerical ones can be reduced using an improved friction law. The implementation of a new friction law is out of the scope of the present work).

The discrepancies detected between the experimental results and the numerical results from the PFEM are not out of the ordinary if we compare with the results obtained with commercial codes (see Rodriguez et al. (2013) for a comparison between PFEM and some commercial codes).

8. Conclusions

In this work we have assembled several numerical techniques within the Particle Finite Element Method (PFEM) in order to face the simulation of continuous chip formation in metal cutting processes. The presented extension of the PFEM includes the use of large strain J_2 plasticity with non-linear thermal softening, a novel Implicit-Explicit (Impl-Ex) solver for the thermo-mechanical coupled problem, and a continuous reconnection of the particles in its updated configuration using *Delaunay* triangulation. The new ingredients also include the treatment of the contact with rigid and deformable tools considering a full frictional thermo-mechanical coupling. As a result of the combination of these techniques the PFEM is now able to handle the modelling of metal cutting processes which presents a good agreement with experimental tests and a good performance compared with other simulation techniques.

The merits of the formulation in terms of its general applicability have been demonstrated with the analysis of four representative numerical simulations of 2D orthogonal cutting tests. These simulations provide results on chip thickness, contact length, cutting and feed forces, distribution of the strain rate, strains, temperatures, and *von Mises* stress. Experimentally, it is very costly and difficult to measure stresses and temperatures in machining. Therefore the results presented in this work offer an advance in the knowledge of the mechanics of chip formation. The performed study evaluates the effects of different process parameters such as material properties, material constitutive laws and tool geometries. The results show good agreement when are compared with some experimental measures of important interest for the performance of the cutting process. These findings place the PFEM as an excellent candidate for modeling machining problems.

Acknowledgements

The research leading to these results has received funding from the European Research Council under the European Union's Seventh Framework Programme (FP/2007-2013)/ERC Grant Agreement n. 320815, Advanced Grant Project COMP-DES-MAT.

Appendix A. Basic steps of the PFEM

In the PFEM the continuum are modelled using an Updated Lagrangian formulation. This description uses an incremental update of the body configuration. That is, all variables are assumed to be known in the current configuration at time t. The new set of variables is sought for in the next or updated configuration at time $t + \Delta t$. The finite element method (FEM) is used to solve the continuum equations. Hence a mesh discretizing the domain must be generated in order to solve the governing equations in the standard FEM fashion.

Recall that the nodes discretizing the analysis domain are treated as material particles which motion is tracked during the transient solution. This is useful to model the separation of particles from the main domain such as fracture of the chip in metal cutting problems, and to follow their subsequent motion as individual particles with a known density, an initial acceleration and velocity and subject to gravity forces. The mass of a given domain is obtained by integrating the density at the different material points over a domain calculation mesh. Therefore quality of the numerical solution depends on the discretization chosen as in the standard FEM. Within the re-connection of the particles that is performed to obtain the calculation mesh, adaptive mesh refinement techniques will be used to improve the resultant distribution.

For clarity purposes we will define the process starting with the collection or cloud of nodes (C) pertaining to the analysis domain, the volume (V) defining the analysis domain and the mesh (M) discretizing the domain.

A typical solution with the PFEM involves the following steps.

1. Definition of the domain(s) Ω_n in the last converged configuration, $t={}^n t$, keeping existing spatial discretization $\bar{\Omega}_n$.
2. Transference of variables by a smoothing process from Gauss points to nodes.
3. Discretization of the given domain(s) in a set of particles of infinitesimal size elimination of existing connectivities $\bar{\Omega}_n$.
4. Reconstruction of the mesh through a triangulation of the domains convex-hull and the definition of the boundary applying the α-shape method (Edelsbrunner and Mucke, 1994), defining a new spatial discretization.
5. A contact method to recognize the multibody interaction.
6. Transference of information, interpolating nodal variables into the Gauss points.
7. Solution of the system of equations for ${}^{n+1}t = {}^n t + \Delta t$.
8. Go back to step 1 and repeat the solution process for the next time step.

Appendix B. The Polynomial pressure projection

The PPP uses a projection on a discontinuous space and as a consequence it does not require specification of a mesh dependent stabilization parameter or calculation of higher-order derivatives.

The implementation of the PPP reduces to a simple modification of the weak continuity equation (incompressibility constraint). In this work, we use the PPP to solid mechanics problems involving large strains.

Given a function $p \in L_2$, the L_2 projection operator $\check{p} : L_2 \to Q^0$ is defined by

$$\int_{V_t} \check{q}\,(p - \check{p})\,dV_t = 0 \quad \forall \check{q} \in Q^0 \tag{39}$$

where $\check{p}$ is the best approximation of the pressure p in the space of polynomials of order $\mathcal{O}(Q^0)$. V_t is the volume of the domain at the current configuration. To stabilize the mixed form given by Eqs. (2), we add the projection operator to the second equation in (2)

$$\int_{V_t} (q - \check{q})\,\frac{\alpha_s}{\mu}\,(p - \check{p})\,dV_t = 0 \tag{40}$$

where α_s is the stabilization parameter and μ is the material shear modulus.

References

Arrazola, P.J., 2003. Modelisation numerique de la coupe: etude de sensibilite des parametres d'entree et identification du frottement entre outil-copeau. L'École Centrale de Nantes, l'Université de Nantes, France Doctoral thesis.
Arrazola, P.J., Ugarte, D., Dominguez, X., 2008. A new approach for the friction identification during machining through the use of finite element modeling. Int. J. Mach. Tools Manuf. 48, 173–183.
Bochev, P.B., Dohrmann, C.R., Gunzburger, M.D., 2008. Stabilization of low-order mixed finite elements for the Stokes equations. SIAM J. Numer. Anal. 44, 82–101.
Bonet, J., Wood, R.D., 1997. Nonlinear Continuum Mechanics for Finite Element Analysis. Cambridge University Press: United Kingdom.
Čanadija, M., Brnić, J., 2004. Associative coupled thermoplasticity at finite strain with temperature-dependent material parameters. Int. J. Plast. 20, 1851–1874.
Carbonell, J.M., 2009. Modeling of Ground Excavation with the Particle Finite Element Method. Phd thesis. Universitat Politècnica de Catalunya (UPC), Barcelona.
Childs, T.H.C., Maekawa, K., Obikawa, T., Yamane, Y., 2000. Metal Machining: Theory and Applications.. Arnold: Great Britain.
Chiumenti, M., Valverde, Q., Saracibar, C.A.d., Cervera, M., 2002. A stabilized formulation for incompressible elasticity using linear displacement and pressure interpolations. Comput. Methods Appl. Mech. Eng. 191, 5253–5264.

Chiumenti, M., Valverde, Q., Saracibar, C.A.d., Cervera, M., 2003. A stabilized formulation for incompressible plasticity using linear triangles and tetrahedra. Int. J. Plast. 20, 1487–1504.
Chorin, A.J., 1997. A numerical method for solving incompressible viscous flow problems. J. Comput. Phys. 135, 118–125.
Cremonesi, M., 2010. A Lagrangian Finite Element Method for the Interaction between Flexible Structures and Free Surfaces Flows. Phd thesis. Politecnico di MIlano, Milan.
Cremonesi, M., Ferrara, L., Frangi, A., Perego, U., 2010a. Simulation of the flow of fresh cement suspensions by a Lagrangian finite element approach. J. Non-Newtonian Fluid Mech. 165, 1555–1563.
de Saracibar, C.A., 1998. Numerical analysis of coupled thermomechanical frictional contact problems. Computational model and applications. Arch. Comput. Methods Eng. 5, 243–301.
Delaunay, B.N., 1934. Sur la Sphère Vide, A la memoire de Georges Voronoi. Otdelenie Matematicheskii i Estestvennyka Nauk 7, 793–800.
Dohrmann, C.R., Bochev, P.B., 2004. A stabilized finite element method for the Stokes problem based on polynomial pressure projections. Int. J. Numer. Methods Fluids 46, 183–201.
Edelsbrunner, H., Mucke, E.P., 1994. Three dimensional alpha shapes. ACM Trans. Graphics 13, 43–72.
Filice, L., Micari, F., Rizzuti, S., Umbrello, D., 2006. A critical analysis on the friction modelling in orthogonal machining. Int. J. Mach. Tools Manuf. 47, 709–714.
Franci, A., 2015. Unified Lagrangian Formulation for Fluid and Solid Mechanics, Fluid-Structure Interaction and Coupled Thermal Problems using the PFEM. Phd thesis. Universitat Politècnica de Catalunya (UPC), Barcelona.
Gadala, M.S., 2004. Recent trends in ALE formulation and its applications in solid mechanics. Comput. Methods Appl. Mech. Eng. 193, 4247–4275.
Gadala, M.S., Movahhedy, M.R., Wang, J., 2002. On the mesh motion for ALE modeling of metal forming processes. Finite Elem. Anal. Des. 38, 435–459.
Ibrahimbegovic, A., Chorfi, L., 2002. Covariant principal axis formulation of associated coupled thermoplasticity at finite strains and its numerical implementation. Int. J. Solids Struct. 39, 499–528.
Idelsohn, S.R., Oñate, E., Pin, F.D., 2004. The particle finite element method: a powerful tool to solve incompressible flows with free-surfaces and breaking waves. Int. J. Numer. Methods Eng. 61, 964–989.
Johnson, G.H., Cook, W.H., 1983. A constitutive model and data for metals subjected to large strains high strain rates and high temperatures. In: Proceedings of the 7th Symposium on Ballistics, 21, pp. 541–547. the Hague, the Netherlands
Limido, J., Espinosa, C., Salan, M., Lacome, J.L., 2007. SPH method applied to high speed cutting modelling. Int. J. Mech. Sci. 49, 898–908.
Marusich, T.D., Ortiz, M., 1995. Modelling and simulation of high-speed machining. Int. J. Numer. Methods Eng. 38, 3675–3694.
Oñate, E., Celigueta, M.A., Idelsohn, S.R., 2006. Modeling bed erosion in free surface flows by the particle finite element method. Acta Geotech. 1, 237–252.
Oñate, E., Idelsohn, S.R., Celigueta, M.A., Rossi, R., 2008. Advances in the particle finite element method for the analysis of fluid-multibody interaction and bed erosion in free surface flows. Comput. Methods Appl. Mech. Eng. 197, 1777–1800.
Oñate, E., Rojek, J., Taylor, R.L., Zienkiewicz, O.C., 2004. Finite calculus formulation for incompressible solids using linear triangles and tetrahedra. Int. J. Numer. Methods Eng. 59, 1473–1500.
Oliver, J., Cante, J.C., Weyler, R., González, C., Hernández, J., 2007. Particle finite element methods in solid mechanics problems. Comput. Methods Appl. Sci. 7, 87–103.
Oliver, J., Huespe, A.E., Cante, J.C., 2008. An implicit/explicit integration scheme to increase computability of non-linear material and contact/friction problems. Comput. Methods Appl. Mech. Eng. 197, 1865–1889.
Olovsson, L., Nilsson, L., Simonsson, K., 1999. An ALE formulation for the solution of two-dimensional metal cutting problems. Comput. Struct. 72, 497–507.
Özel, T., 2006. The influence of friction models on finite element simulations of machining. Int. J. Mach. Tools Manuf. 46, 518–530.
Peri, D., Owen, D.R.J., 1999. Computational techniques applied to high-speed machining under adiabatic strain localization conditions. Comput. Methods Appl. Mech. Eng. 171, 445–461.
Rakotomalalan, R., Joyot, P., Touratier, M., 1993. Arbitrary Lagrangian–Eulerian thermomechanical finite-element model of material cutting. Commun. Numer. Methods Eng. 9, 975–987.
Rodriguez, J.M., 2014. Numerical Modeling of Metal Cutting Processes using the Particle Dinite Element Method(PFEM). Phd thesis. Universitat Politècnica de Catalunya (UPC), Barcelona.
Rodriguez, J.M., Arrazola, P.J., Cante, J.C., Kortabarria, A., Oliver, J., 2013. A sensibility analysis to geometric and cutting conditions using the particle finite element method (PFEM). Procedia CIRP 8, 105–110.
Rodriguez, J.M., Cante, J.C., Oliver, J., 2015. On the numerical modelling of machining processes via the Particle Finite Element Method (PFEM). In: CIMNE, 156, p. 186. Barcelona
Rodriguez, J.M., Carbonell, J.M., Cante, J.C., Oliver, J., 2016. The particle finite element method (PFEM) in thermomechanical problems. Int. J. Numer. Methods Eng doi:10.1002/nme.5186.
Saracibar, C.A.d., Chiumenti, M., Valverde, Q., Cervera, M., 2006. On the orthogonal subgrid scale pressure stabilization of finite deformation J2 plasticity. Comput. Methods Appl. Mech. Eng. 195, 1224–1251.
Sekhon, G.S., Chenot, J.L., 1993. Numerical simulation of continuous chip formation during non-steady orthogonal cutting simulation. Eng. Comput. 10 (1), 31–48.
Shewchuk, J.R., 1998. A condition guaranteeing the existence of higher-dimensional constrained Delaunay triangulations. In: Proceedings of the Fourteenth Annual Symposium on Computational Geometry, ACM, Minneapolis, MN, USA, pp. 76–85.
Simo, J.C., 1988a. A framework for finite strain elastoplasticity based on maximum plastic dissipation and the multiplicative decomposition: Part I. Continuum formulation. Comput. Methods Appl. Mech. Eng. 666, 199–219.
Simo, J.C., 1988b. A framework for finite strain elastoplasticity based on maximum plastic dissipation and the multiplicative decomposition. Part II: Computational aspects. Comput. Methods Appl. Mech. Eng. 68, 1–31.
Simo, J.C., Hughes, T.J.R., 1998. Computational Inelasticity. Springer-Verlag: New York.
Simo, J.C., Miehe, C., 1992. Associative coupled thermoplasticity at finite strains: formulation, numerical analysis and implementation. Comput. Methods Appl. Mech. Eng. 98, 41–104.
Svoboda, A., Wedberg, D., Lindgren, L.E., 2010. Simulation of metal cutting using a physically based plasticity model. Modell. Simul. Mater. Sci. Eng. 18, 123–131.
Voce, E., 1955. A practical strain hardening function. U.K.: Metall. Br. J. Metals 51, 219–226.
Wriggers, P., Simo, J.C., 1985. A note on tangent stiffness for fully nonlinear contact problems. Commun. Appl. Numer. Methods 1, 199–203.
Zienkiewicz, O.C., Zhu, J.Z., 1992a. The superconvergent patch recovery and a posteriori error estimates. Part 1: The recovery technique. Int. J. Numer. Methods Eng. 33, 1331–1364.
Zienkiewicz, O.C., Zhu, J.Z., 1992b. The superconvergent patch recovery and a posteriori error estimates. Part 2: Error estimates and adaptivity. Int. J. Numer. Methods Eng. 33, 1365–1382.